Master Thesis

Polarized Raman spectra of Weyl semimetal TaP

(ワイル半金属TaPの分極ラマンスペクトル)

Pang Xiaoqi

Department of Physics
Graduate School of Science
Tohoku University

July, 2020

Acknowledgments

It is a hard-won opportunity to thank the people who supported me a lot in the last two years. First, I thank my supervisor, Saito-sensei, for giving nice lectures, discussing and providing suggestions for my research. He is always active and hard working, that embraves me a lot when I was lazy. I express my gratitude to the collaborators Kunyan Zhang and Prof. Shengxi Huang in Pennsylvania University for their great efforts in the present collaboration. I would like to thank Dr. A. R. T. Nugraha for teaching everything patiently when I was a fresh man in the laboratory. I also thank Dr. N. T. Hung, who alway helped me not only in research but also for confusions about culture difference. And Ms. T. Wang, my friend and colleague, supported me a lot in last two years. Additionally, I say thank you to the members in this laboratory: Dr. M. S. Ukhtary, Dr. Wang Sake, Mr. F. Pratama, Mr. Maruoka Masato, Mr. Tian Yuan.

I am very thankful to International Joint Gratuate Program in Materials Science (GP-MS Program) in Tohoku University for financially supporting my study. I also would like to thank the International Graduate Program for Advanced Science (IG-PAS) in Tohoku University.

Finally, I am quite grateful to my family. Without the financial and mental support from my family, I will not achieve this thesis. I also say thanks to my friends in Japan for enriching my life and keeping me healthy mentally.

Contents

Chapter 1

Introduction

1.1 Purpose of the study

Topological Weyl semimetal (WSM) is a new class of topological materials that realize the Weyl fermion in condensed matter systems, i.e., a massless solution to the Dirac equation with a definite chirality. In a WSM, the linear energy dispersion and nontrivial Berry phases in the band structure lead to chiral magneto-transport phenomena, such as (1) large magnetoresistance (MR) (850,000% at 1.85 K in a magnetic field of up to 9 T for NbP [1]) that is much larger than that in normal metals and semiconductors, and (2) high mobility [1] as in classical semimetals such as graphite. Such exotic properties suggest great potential for applications. The high mobility and the large MR make the possibility for employing WSM in high-speed electronics and spintronics. Moreover, surface states of the WSMs can also play a role in surface-related chemical processes like catalysis. In experiments, although many materials have been predicted as WSM, only several materials have been proved as WSM through angle-resolved photoemission spectroscopy (ARPES). So far, TaAs, TaP, NbAs and NbP [2, 3, 4] are classified as type-I WSM, in which the Fermi surface shrinks to a point at the Weyl point. While the layered transition-metal dichalcogenides WTe_2 and $MoTe_2$ [5, 6] are classified as type-II, where the Weyl cone is tilted. In this work, we focus on TaP, the typical type-I WSM. In the experiments conducted by Kunyan Zhang and Shengxi Huang, who are our collaborators, several interesting phenomena exist in the angle-resolved polarized Raman spectra of TaP. The purpose of the thesis is to understand physics of polarized Raman spectra of TaP by first principles calculations.

In Raman spectroscopy, we study the light-matter interactions including electron-photon, electron-phonon, and electron-electron interactions. The Raman spectra provide abundant information on electronic structure, phonon and crystal symmetry of the materials. Such information is important for the WSM, since the broken inversion symmetry and electronic gapless energy dispersion are a prerequisite of the WSM.

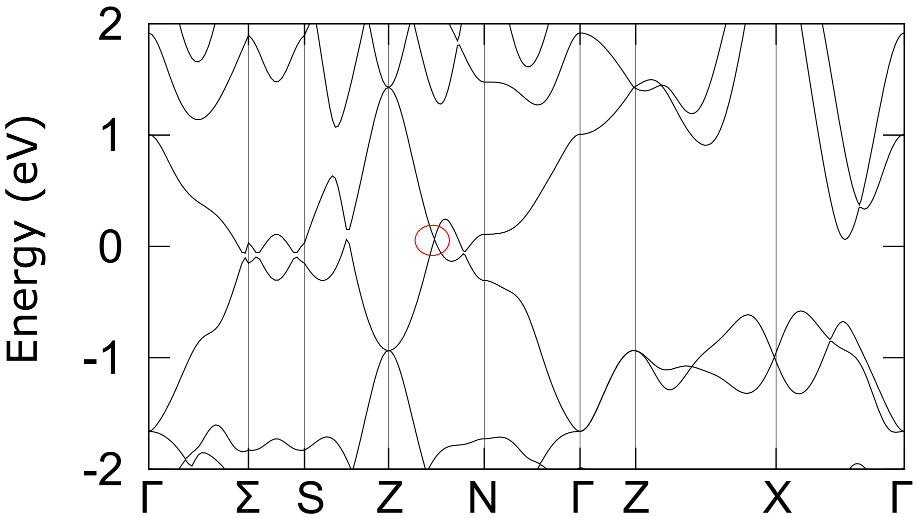

Figure 1.1 Electronic band structure of TaP. At the point that is red-line circled in the path between Z and N, valence and conduction bands touch at Fermi level.

Recently, several studies about the WSM have been carried out by using Raman spectroscopy. Liu et al. [7] reported angle-resolved polarized Raman spectroscopy of WSM $TaIrTe_4$ in which a strong in-plane optical anisotropy is observed. In another work [8], the phase transition of orthorhombic $MoTe_2$, a type-II WSM, is observed by the emergence of new modes in the Raman spectra.

1.2 Organization

The thesis is organized into 4 chapters. In the remaining part of chapter 1, we introduce present the background of this study, including basic concept and properties of Weyl semimetal and Raman spectroscopy, experimental results of polarized Raman spectroscopy for TaP. In Chapter 2, we explain the methods to calculate the Raman intensity. In Chapter 3, we present and discuss the calculated results of polarized Raman spectroscopy of TaP. In Chapter 4, a summary of this thesis is given.

1.3 Backgrounds

1.3.1 Topological Weyl semimetal

Recently, Topological materials have attracted a lot of attentions because of their exotic properties, which are highlighted by topology. Topology is a concept from

---

Fig. 1.1: Fig/ch1-bnd.pdf
Fig. 1.2: Fig/ch1-weyltype.pdf
Fig. 1.3: Fig/ch1-fermiarc.pdf

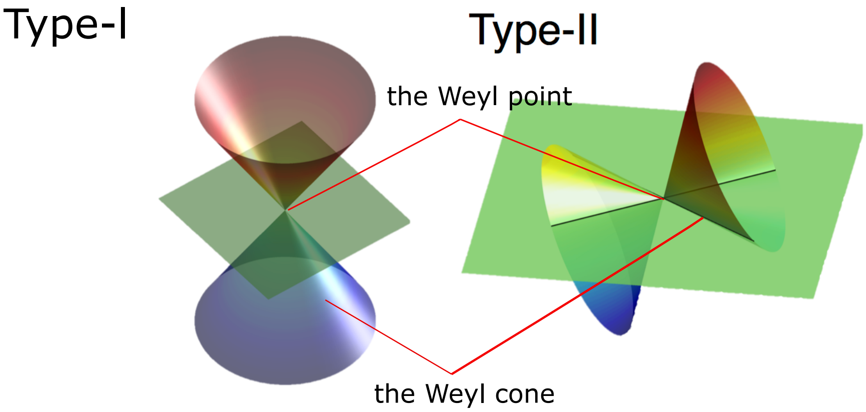

Figure 1.2 For the type-I WSM, the Fermi surface shrinks to zero at the Weyl point. The type-II WSM shows the tilting of the Weyl cone [9].

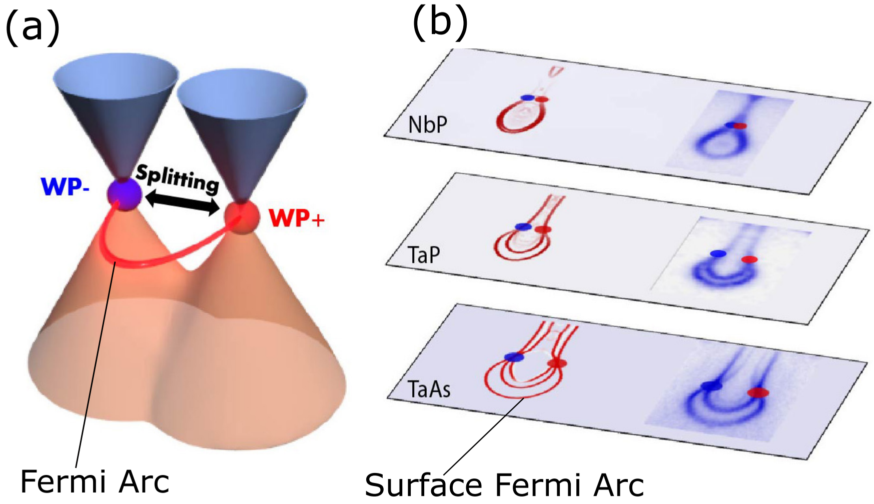

Figure 1.3 (a) Red and blue indicate the different chiralities of the Weyl points (W+ and W-), which are connected by the exotic surface Fermi arc (red curve). (b) Theoretical calculation and experimental observation of the evolution of Weyl points and surface Fermi arcs in three compounds of the family [10].

mathematics in which a property of the object is invariant for any deformation. Materials with the properties that are invariant for a topological transformation is called topological materials. According to whether the valence and conduction bands touch at the Fermi level or not, topological materials can be classified, respectively, as topological insulators or topological semimetals. Furthermore, if the energy band is non-degenerate, topological semimetal is called the WSM. If the energy bands are doubly degenerate, topological semimetal is called the topological Dirac semimetal.

Let us focus on the WSM. In 1929, Hermann Weyl proved the existence of a Weyl fermion, a massless fermion in the Dirac equation in the high energy physics [11]. The Weyl fermions have remained undiscovered until 2015 scientists found that the Weyl fermion exists in a low-energy excitation of the Weyl semimetal [12, 13, 2, 3, 4]. Up to now, several materials have been discovered as the Weyl semimetals in which the Weyl points, the Fermi arcs, the chiral-anomaly-induced negative MR [14, 15], and the anomalous Hall effect (AHE) [5] has been observed. TaP belongs to the type-I WSM that is characterized by the fact that the conduction and valence bands cross at the Fermi level in the bulk band structure. In Fig 1.2, we show the schematics of the type-I and type-II WSM. There are several features for the WSM. First, the Weyl points, where the conduction and valence bands touch each other, can be seen clearly in the energy band structure as shown in Fig 1.1. Moreover, the band structure shows a linear energy dispersion near the Weyl points. A physical meaning of the Weyl point is explained by the Berry curvature, $\overrightarrow{\Omega_n}(k) = \overrightarrow{\nabla_k} \times i\langle n(k)|\overrightarrow{\nabla_k}|n(k)\rangle$, that is a pseudo-vector calculated by the wave-function $|n(k)\rangle$ in the K-space. If we take an integral on k over the Fermi surface including the Weyl point, the integration gives either 2π or -2π, which defines the chirality of the Weyl point. Second, the monopole feature of the Weyl point leads to another important feature of WSM, that is Fermi arcs. Fermi arcs is a surface projection of a two dimensional Fermi contour and it exhibits an unclosed line that starts from one Weyl point and ends at the other with opposite chirality. Scanning Fermi arcs through ARPES and scanning tunneling spectroscopy (STS) is the important way to identify WSM in experiments. Finally, the linear energy dispersion and nontrivial Berry phase in the band structure cause the chiral magneto-transport phenomena, the large MR, and the high mobility. Recently, a negative longitudinal MR has been reported in the two types of WSMs (TaAs [14, 15], TaP [16] and NbP) and with a very high mobility (5×10^6 cm^2/(v.sec)) in NbP [1]) compared with classical semimetals such as graphite (2×10^4 cm^2/(v.sec)).

1.3.2 The Raman spectroscopy

1.3.2.1 The First-order Raman scattering process

The Raman spectroscopy is one of widely-used optical techniques in the material science, that can be used to detect isotopes [17], structural phases, defects [18], local strain [19]. Further information on the electronic structure can be obtained by means of the resonant Raman spectroscopy. The Raman spectroscopy became very popular in the 1960s when the laser was discovered as a coherent light source. On the other hand, compared with the other techniques such as scanning electron microscope (SEM), the Raman spectroscopy can characterize materials without destroying the materials. The First-order Raman scattering consists of (1) the absorption of a photon, (2) the emission or absorption of a phonon, and (3) the emission of a photon as shown in

---

Fig. 1.4: Fig/ch1-raman-process.pdf

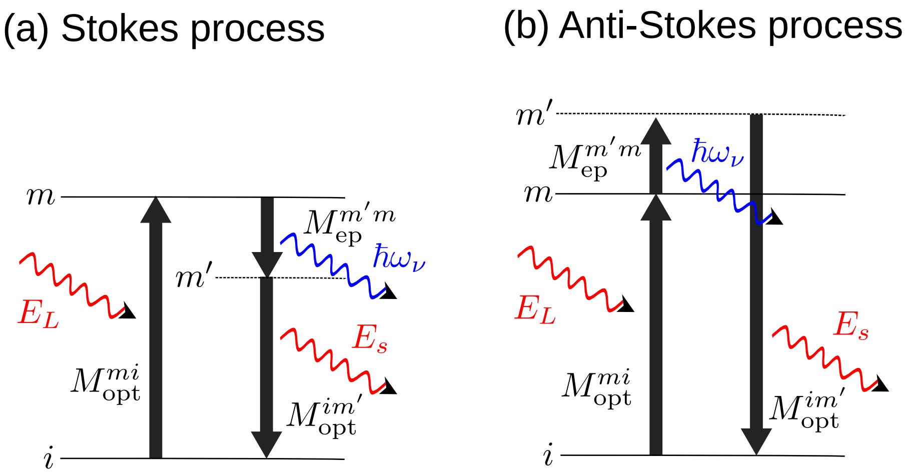

Figure 1.4 First-order Raman scattering process process for (a) Stokes and (b) Anti-Stokes Raman scattering. E_L, E_s, and $\hbar\omega_\nu$ are the energy of the incident laser, scattered light, emitted (absorbed) phonon, respectively. The M_{opt}^{fi} (M_{ep}^{fi}) indicates the electron-photon (electron-phonon) matrix element from the i to f state.

Fig. 1.4. The case of phonon emission is called the Stokes Raman, while the case of phonon absorption is called the anti-Stokes Raman. The difference between the wave number of incident laser and the scattered laser is called the Raman shift, that is equal to the wave number of the emitted (or absorbed) phonons in Stokes (or anti-Stokes) Raman. In Fig. 1.4 we show the schematic picture of the process of the (a) Stokes ((b) anti-Stokes) first order Raman scattering, in which only one phonon is emitted (absorbed). The incident photon interacts with an electron in the valence band (state i) by electron-photon interaction $M_{\rm opt}^{mi}$ and the electron is excited to the conduction band (state m). Then the photon-excited electron interacts with a phonon by the electron-phonon interaction $M_{\rm ep}^{m'm}$ and the electron moves to the intermediate state m'. Finally, the electron goes back from the m' state to the original i state in the valence band with emitting a photon by electron-photon interaction $M_{\rm opt}^{im'}$. When the energy of incident light (scattered light) equals to the energy difference between initial state and final state that is $E_L = E_{mi}$ ($E_s = E_{m'i}$), the intensity of Raman spectroscopy is significantly enhanced in the experiment. The enhanced Raman scattering is called resonant Raman scattering.

1.3.2.2 The polarized Raman spectroscopy

For a material with low symmetrical structure, the Raman intensity depends on the polarization of light. By rotating polarization directions of the incident light and the scattered light independently, we obtain polarized Raman spectra, which provide

---

Fig. 1.5: Fig/ch1-polar-raman.pdf

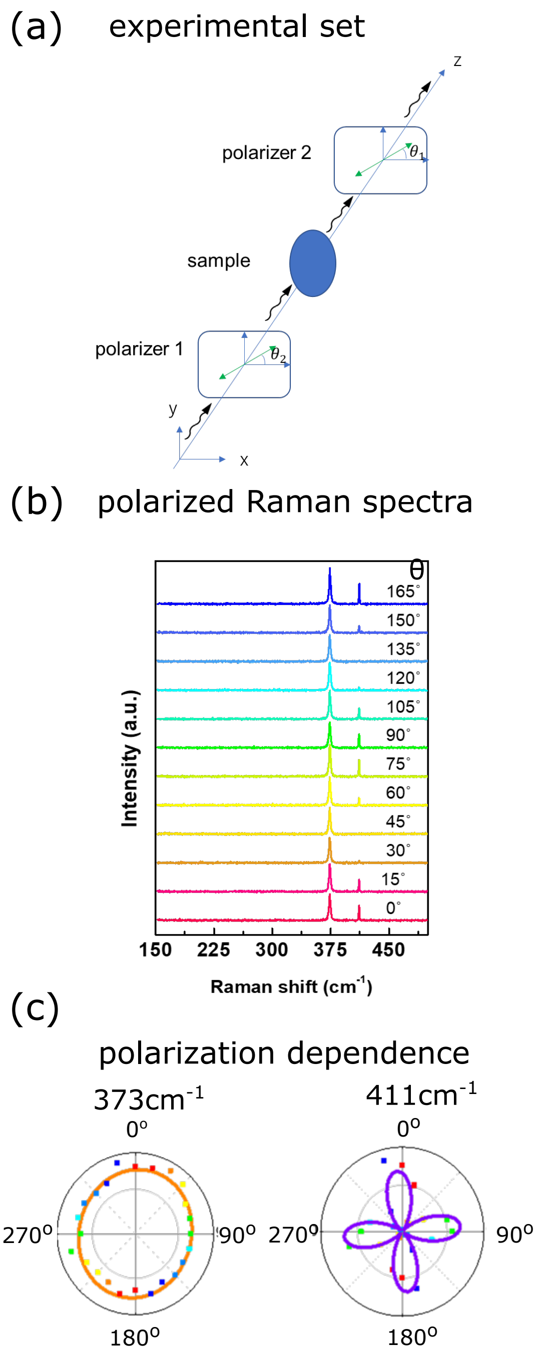

Figure 1.5 (a) experimental set (b) polarized Raman spectra and (c) polar plot of the Raman intensity. The experimental set is parallel (HH) configurations with $\theta_1 = \theta_2$. By rotating polarizer 1 and 2, we obtain Raman spectra as function of θ. If we plot Raman intensity by θ, we can get the polarization dependence with symmetries

more detailed information on the symmetry of phonon than that from resonant Raman spectroscopy. In the usual polarized Raman experiments, linearly polarized light is obtained by a polarizer. There are two typical geometries of the polarization, that is, parallel (HH) and perpendicular (HV) configurations. The polarization direction of the incident and scattered light are parallel (perpendicular) each other for the HH (HV) configuration. By rotating the polarizers in the parallel configuration ($\theta = \theta_1 = \theta_2$) as shown in Fig. 1.5 (a), we obtain the HH-polarized Raman spectra as a function of θ relative to the sample, as shown in Fig. 1.5 (b). There are two typical peaks in the polarized Raman spectra that are located at 373 cm^{-1} and 411 cm^{-1} Raman shift. If we plot the Raman intensity as a function of θ for 373 cm_{-1} and 411 cm^{-1} Raman shifts respectively, we obtain the polar plot of the Raman intensity as shown in Fig. 1.5 (c). For 373 cm^{-1} Raman shift, the Raman intensity does not show obvious enhancement for a specific value of θ, while the Raman intensity is maximum when $\theta = 75, 165, 255,$ or 345 degree. The intensity of polarized Raman spectra as a function of θ provides the symmetry of emitted (absorbed) phonon in the Raman scattering, which help us to identify the structure of the materials. Furthermore, compared with the conventional Raman spectroscopy in which many polarizations of the scattered light are mixed in the signal, the polarized Raman spectroscopy provides the polarized signal. In such a way, the signal has more information. For example, the Raman peak split by an isotope in the materials can be observed in the polarized Raman spectroscopy [20] but not in the conventional Raman spectroscopy.

1.3.3 The polarized Raman spectra for TaP

1.3.3.1 The theoretical analysis

Let us analyze the symmetries for phonon modes of TaP by Raman tensor theory, in which the Raman intensity for ν phonon mode $I_{\mathrm{Raman}}(\nu)$ is given by

$$I_s(\nu) = \left| \boldsymbol{P}_s^* \overleftrightarrow{R}(\nu) \boldsymbol{P}_i \right|^2 , \tag{1.1}$$

where $\boldsymbol{P}_i$ ($\boldsymbol{P}_s$) and $\overleftrightarrow{R}(\nu)$ are the polarization vector of incident (scattered) light and the Raman tensor for the ν phonon mode, respectively. Here we consider the $\mathrm{Z(XX)\overline{Z}}$ configuration that the polarization vectors for incident and scattered light are parallel to each other and the linearly-polarized light propagates in z-direction with electronic field in X-direction corresponding to $\theta = 0$. Then, the polarization vectors for the parallel configuration are written as,

$$\boldsymbol{P}_i = \boldsymbol{P}_s = \begin{pmatrix} \cos\theta \\ \sin\theta \\ 0 \end{pmatrix} , \tag{1.2}$$

Fig. 1.6: Fig/ch1-tapstru.pdf
Fig. 1.7: Fig/ch1-c4v.pdf

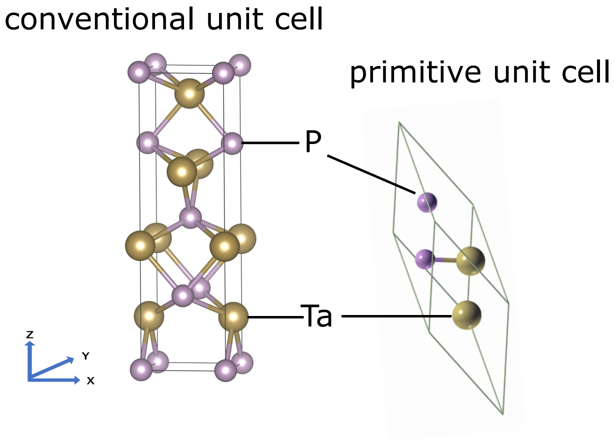

Figure 1.6 Crystal structure of TaP. The left figure is the conventional unit cell that shows TaP belongs to the body-centered tetragonal space group $I4_1md$ (No. 109) (point group C_{4v}). The right figure is primitive unit cell that consists of two Ta and two P atoms. Therefore, it has twelve phonon modes in which three acoustic phonon modes are [A_1+E] modes, and nine optical phonon modes are [A_1+2B_1+3E] modes.

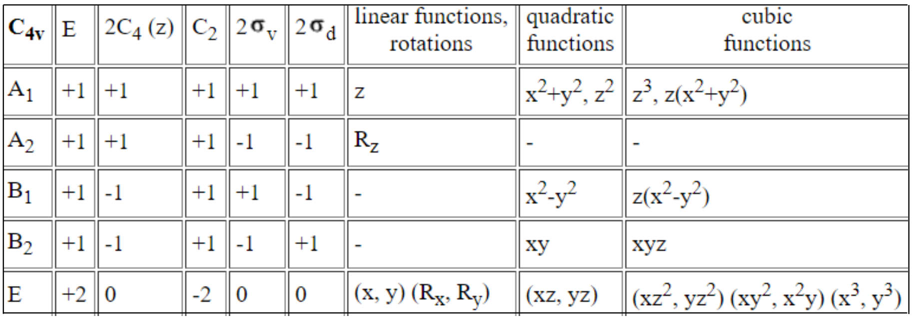

C_{4v}	E	$2C_4$ (z)	C_2	$2\sigma_v$	$2\sigma_d$	linear functions, rotations	quadratic functions	cubic functions
A_1	+1	+1	+1	+1	+1	z	x^2+y^2, z^2	z^3, $z(x^2+y^2)$
A_2	+1	+1	+1	-1	-1	R_z	-	-
B_1	+1	-1	+1	+1	-1	-	x^2-y^2	$z(x^2-y^2)$
B_2	+1	-1	+1	-1	+1	-	xy	xyz
E	+2	0	-2	0	0	(x, y) (R_x, R_y)	(xz, yz)	(xz^2, yz^2) (xy^2, x^2y) (x^3, y^3)

Figure 1.7 Character table for C_{4v} point group. There are 5 irreducible representations A_1, A_2, B_1, B_2 and E, in which A_1, B_1, B_2 and E with quadratic functions are Raman active.

where θ is the polarization angle of the light relative to the x axis in xy plane. The Raman tensors $\overleftrightarrow{R}(\nu)$ for phonon modes can be obtained from the character table once we know the crystal structure of the material. TaP belongs to body-centered tetragonal space group $I4_1md$ (No. 109, C_{4v}) as shown in Fig. 1.6. Since there are two Ta and two P atoms in the primitive unit cell of TaP, it has twelve phonon modes in which three acoustic phonon modes are A_1 and doubly degenerated E modes, and nine optical phonon modes are A_1, two B_1 and three doubly degenerated E modes. According to the character table of C_{4v} point group in Fig. 1.7, both A_1, B_1 and E modes are Raman active because they have quadratic functions. We can write down the Raman tensors for each modes according to their quadratic functions. The general

Raman tensor is written as $\begin{pmatrix} x^2 & xy & xz \\ yx & y^2 & yz \\ zx & zy & z^2 \end{pmatrix}$. Thus, the Raman tensor for A$_1$, B$_1$ and E modes are written as follows:

$$\begin{aligned}
\overleftrightarrow{R}(A_1) &= \begin{pmatrix} a & 0 & 0 \\ 0 & a & 0 \\ 0 & 0 & c \end{pmatrix} \\
\overleftrightarrow{R}(B_1) &= \begin{pmatrix} a & 0 & 0 \\ 0 & -a & 0 \\ 0 & 0 & 0 \end{pmatrix} \\
\overleftrightarrow{R}(E) &= \begin{pmatrix} 0 & 0 & 0 \\ 0 & 0 & a \\ 0 & a & 0 \end{pmatrix} or \begin{pmatrix} 0 & 0 & a \\ 0 & 0 & 0 \\ a & 0 & 0 \end{pmatrix} \qquad (1.3)
\end{aligned}$$

The Raman intensity of the A$_1$ mode is calculated as follows:

$$\begin{aligned}
I_s(A_1) &= \left| \begin{pmatrix} \cos\theta & \sin\theta & 0 \end{pmatrix} \begin{pmatrix} a & 0 & 0 \\ 0 & a & 0 \\ 0 & 0 & c \end{pmatrix} \begin{pmatrix} \cos\theta \\ \sin\theta \\ 0 \end{pmatrix} \right|^2 \\
&= |a|^2, \qquad (1.4)
\end{aligned}$$

so the A$_1$ mode intensity does not have θ dependence. The Raman intensities for B_1 mode is written as,

$$\begin{aligned}
I_s(B_1) &= \left| \begin{pmatrix} \cos\theta & \sin\theta & 0 \end{pmatrix} \begin{pmatrix} a & 0 & 0 \\ 0 & -a & 0 \\ 0 & 0 & 0 \end{pmatrix} \begin{pmatrix} \cos\theta \\ \sin\theta \\ 0 \end{pmatrix} \right|^2 \\
&= \left| a\cos^2\theta - a\sin^2\theta \right|^2 = a\cos 2\theta \qquad (1.5)
\end{aligned}$$

which suggests that the polarization dependence of B_1 phonon mode has four-fold symmetry. The Raman intensities for E mode is written as,

$$\begin{aligned}
I_s(E) &= \left| \begin{pmatrix} \cos\theta & \sin\theta & 0 \end{pmatrix} \begin{pmatrix} 0 & 0 & a \\ 0 & 0 & 0 \\ a & 0 & 0 \end{pmatrix} \begin{pmatrix} \cos\theta \\ \sin\theta \\ 0 \end{pmatrix} \right|^2 \\
&= \left| \begin{pmatrix} 0 & 0 & a\cos\theta \end{pmatrix} \begin{pmatrix} \cos\theta \\ \sin\theta \\ 0 \end{pmatrix} \right|^2 = 0 \\
\mathit{or} & \\
I_s(E) &= \left| \begin{pmatrix} \cos\theta & \sin\theta & 0 \end{pmatrix} \begin{pmatrix} 0 & 0 & 0 \\ 0 & 0 & a \\ 0 & a & 0 \end{pmatrix} \begin{pmatrix} \cos\theta \\ \sin\theta \\ 0 \end{pmatrix} \right|^2 \\
&= \left| \begin{pmatrix} 0 & 0 & a\sin\theta \end{pmatrix} \begin{pmatrix} \cos\theta \\ \sin\theta \\ 0 \end{pmatrix} \right|^2 = 0,
\end{aligned} \tag{1.6}$$

so the E mode is not observable in the $Z(XX)\overline{Z}$ configuration.

1.3.3.2 Experimental results of the polarized Raman spectra

Shengxi Huang's group measured the angle-resolved polarized Raman spectroscopy of TaP which is one of WSM for five excitation wavelengths ranging from 364 nm to 785 nm as shown in Fig. 1.8. The Raman active modes, i.e., one A_1 and two B_1 (B_1^1 and B_1^2) phonon modes, exhibit several unique features that cannot be explained by the resonant Raman spectroscopy. In order to distinguish two B_1 modes in TaP, we label them as B_1^1 and B_1^2, where the B_1^2 mode has a higher frequency than the lower B_1^1 mode. First, the polar plot of the Raman intensity show systematic deviation from the prediction of the Raman tensor theory. The B_1^2 mode shows an unusual two-fold symmetry instead of a four-fold symmetry as is seen for the 488, 532, and 633 nm excitations. Second, the Raman peak of the B_1^1 mode is absent for the 633 nm excitation as shown in Fig. 1.9. We will explain the origin of the unique angular dependence by the calculated resonant Raman spectra in this thesis.

Fig. 1.8: Fig/ch1-exp.pdf
Fig. 1.9: Fig/ch1-expspectra.pdf

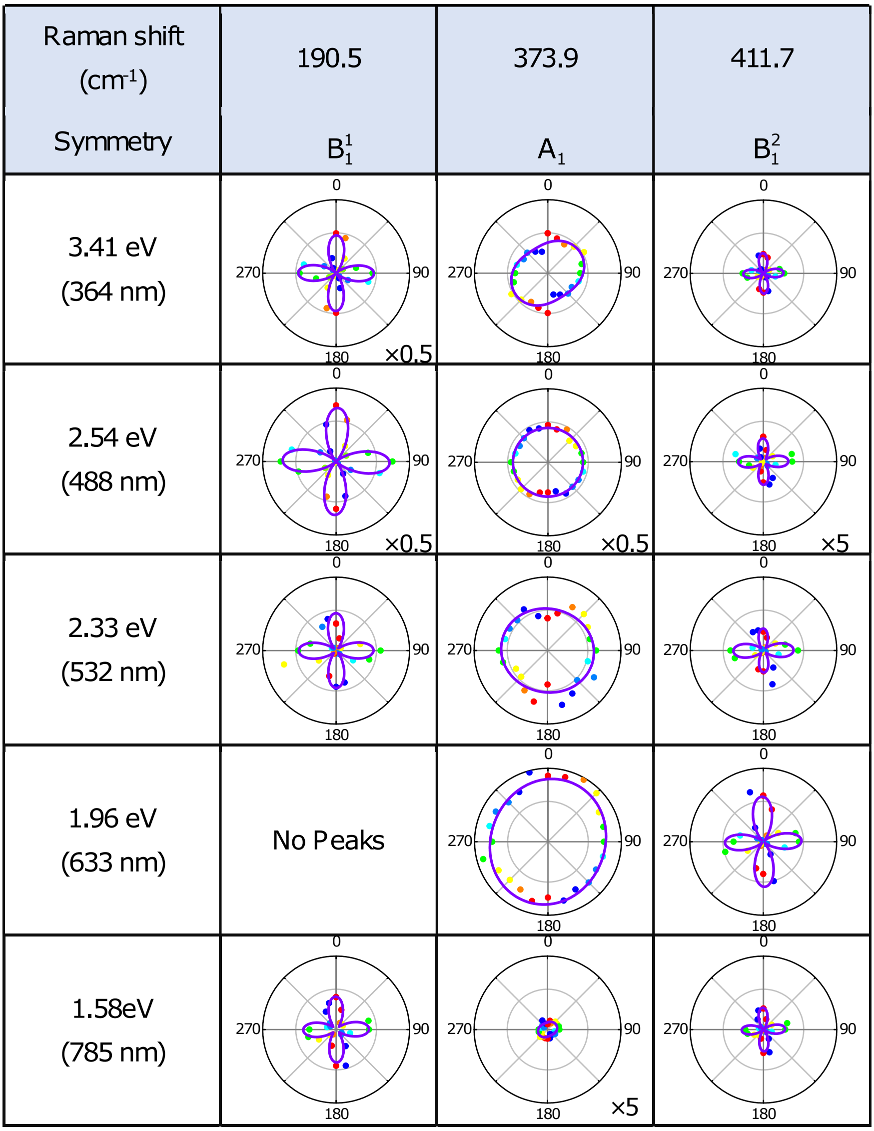

Figure 1.8 Measured polar plots of the B_1^1, A_1 and B_1^2 modes for five excitation wavelengths 364 nm (3.41 eV), 488 nm (2.54 eV), 532 nm (2.33 eV), 633 nm (1.96 eV), 785 nm (1.58 eV) [21].

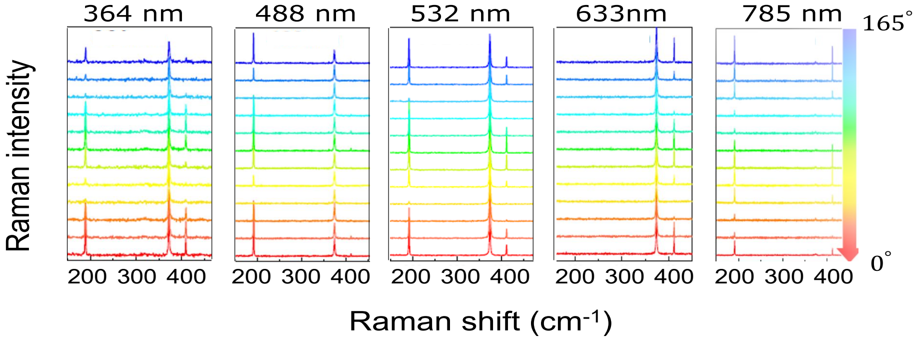

Figure 1.9 Measured polarized Raman spectra of TaP. The figures from left to right corresponds to five excitation wavelengths 364 nm (3.41 eV), 488 nm (2.54 eV), 532 nm (2.33 eV), 633 nm (1.96 eV), 785 nm (1.58 eV). For each excitation, Raman intensity is plotted as the function of Raman shift, and there are three peaks at 190.5 cm^{-1}, 372.9 cm^{-1}, 411.7 cm^{-}1 Raman shift. The color bar at right notes the polarization angle from 0° to 165° [21].

Chapter 2

Theoretical methods

In this chapter, we begin with the formula of Raman intensity for the first-order Raman scattering and how to obtain it by first principles calculations. Then we discuss each subject of the Raman scattering formula that are the the resonance conditions, the electron-photon interaction, and the electron-phonon interaction.

2.1 The Raman intensity for the first-order Raman scattering

2.1.1 The formula of Raman intensity

The Raman intensity for the first-order Raman scattering is calculated as follows:

$$I_s = \sum_{\nu} \left| \sum_{i=f,m,m'} \frac{M_{opt}^{fm'} M_{ep,\nu}^{m'm} M_{opt}^{mi}}{(E_{\mathrm{L}} - E^{mi} - i\gamma)(E_{\mathrm{L}} - E^{m'i} \pm \hbar\omega_{\nu} - i\gamma)} \right|^2, \tag{2.1}$$

where $M_{opt}^{fm'}$, M_{opt}^{mi} are the electron-photon interaction elements that correspond to the process that an electron is excited from valence band (state i) to the conduction band (state m) and that the electron goes back from the m' state to the original i, respectively. $M_{ep,\nu}^{m'm}$ is the electron-phonon interaction element that correspond to the process that the photon-excited electron interacts with a phonon and the electron moves to the intermediate state m'. E_{L}, $\hbar\omega_{\nu}$ are the energy of incident light, and the ν mode phonon, respectively. $E^{m(m')i}$ is the energy difference between the i and $m(m')$ states and γ is resonance window line-width.

The formula of Raman intensity Eq. (2.1) is derived by the third-order time-dependent perturbation theory as shown in appendix B. It is important to note that the formula Eq. (B.27) at the end of appendix B that we obtained from the third-order time-dependent perturbation theory directly has sight difference with Eq. (2.1). In Eq. (2.1), we replace γ_1 and γ_2 by the identical parameter γ. To understand the rationality of such a simplification, we need to back to the physical meaning of parameters γ_1 and γ_2. $\gamma_1 = \hbar\eta_1$ and $\gamma_2 = \hbar(\eta_1 + \eta_2)$, where η_1 and η_2 are the inverse

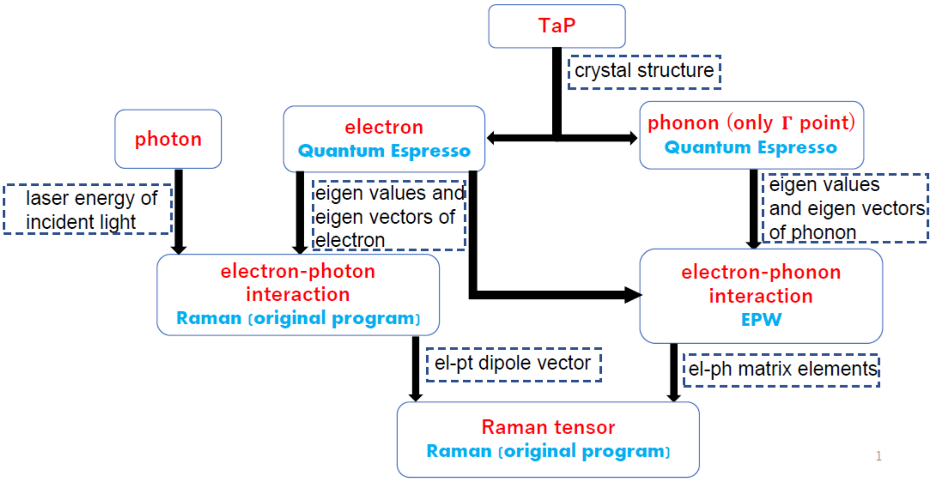

Figure 2.1 The flow chart of first principles calculations. Calculated subjects and the programs(bold) are shown in the solid rectangle. Quantum Espresso [22] and EPW [23] package both are open source software for DFT calculation. Raman is the program developed by ourselves. The outputs to next step is shown in the dotted rectangle.

of the lifetime of photo-excited electron (τ_1) and the phonon (τ_1), respectively. Since τ_1 is sufficiently smaller than τ_1, the difference between γ_1 and γ_2 can be ignored. In conclusion, the value of γ is decided by the lifetime of photo-excited electron.

We focus on the denominator part in Eq. (2.1). If $E_{\rm L} = E^{mi}$ or $E_{\rm L} = E^{m'i} \pm \hbar\omega_\nu$, the Raman intensity gets a large enhancement. The physics meaning is that when the excitation laser energy $E_{\rm L}$ matches the energy difference between the valence (i) and conduction (m) bands E^{mi}, the Raman intensity is increased by many orders of magnitude that means resonant Raman happens. Similarly, when the scattered laser energy $E_{\rm L} \pm \hbar\omega_\nu$ matches the energy difference $E^{m'i}$ between the valence (i) and conduction (m') bands, resonant Raman also happens. We call $E_{\rm L} = E_{mi}$ (resonance with incident light) or $E_{\rm L} = E^{m'i} \pm \hbar\omega_\nu$ (resonance with scattered light) as resonance condition. Another important element in the denominator part is γ, the resonance window line-width. The value of gamma is a important factor to influence the symmetry of the polarized Raman spectra in TaP and we will discuss this in detail in the next chapter. We adapt γ as a parameter in our calculation in order to invest how the values of γ influence the symmetry of the polarized Raman spectra.

2.1.2 The flow chart of first principles calculations

In order to calculate the Raman intensity by using Eq. (2.1), the crystal structure of the material TaP is needed. First, we can obtain the eigen values, eigen vectors

---

Fig. 2.1: Fig/ch2-flowchart.pdf

of the electrons and phonons from Quantum Espresso. The detailed parameters used in Quantum Espresso is shown in appendix A. Second, the electron-photon (el-pt) interaction elements for specific laser energy are calculated by our own program. The electron-phonon (el-ph) interaction elements are calculated by EPW package. The details for el-pt interaction and el-ph interaction are explained in next section. Finally, with el-pt interaction elements and el-ph interaction elements, our own program calculates the Raman tensor. The resonance window line-width γ is adapted as a parameter in the final step of the calculation.

2.2 Electron-photon interaction

In this section, we derivate the electron-photon interaction M_{opt}^{fi} and explain how to calculate it by first-principles calculation.

2.2.1 The derivation of the electron-photon interaction

The Hamiltonian for an electron in the electromagnetic field is explained by

$$\begin{aligned} H &= \frac{1}{2m}(-i\hbar\nabla - e\boldsymbol{A})^2 + V(\boldsymbol{r}) + e\phi \\ &= \frac{1}{2m}(-\hbar^2\boldsymbol{\nabla}^2 - ie\hbar\boldsymbol{\nabla}\cdot\boldsymbol{A} - 2ie\hbar\boldsymbol{A}\cdot\boldsymbol{\nabla} + e^2(\boldsymbol{A})^2) + V(\boldsymbol{r}) + e\phi, \end{aligned} \tag{2.2}$$

where A is the vector potential that defined by $\boldsymbol{B} = \nabla \times \boldsymbol{A}$, and the m, $V(\boldsymbol{r})$ and ϕ are the mass of the electron, crystal potential and static electrostatic potential, respectively. If we take the Coulomb gauge, we get

$$\nabla \cdot \boldsymbol{A} = 0. \tag{2.3}$$

We assume the scalar potential $\phi = 0$, and neglect the second-order term of $\boldsymbol{A}$. Using Eq. (2.3), the Hamiltonian in Eq. (2.2) is given by

$$\begin{aligned} H &= -\frac{\hbar^2}{2m}\boldsymbol{\nabla}^2 + V(\boldsymbol{r}) - \frac{ie\hbar}{m}\boldsymbol{A}\cdot\boldsymbol{\nabla} \\ &= H_0 + H_{opt}, \end{aligned} \tag{2.4}$$

where the unperturbed Hamiltonian H_0 is defined by

$$H_0 = -\frac{\hbar^2}{2m}\boldsymbol{\nabla}^2 + V(\boldsymbol{r}), \tag{2.5}$$

and the perturbation Hamiltonian for electron-photon interaction H_{opt} is explained by

$$H_{opt} = -\frac{ie\hbar}{m}\boldsymbol{A}\cdot\boldsymbol{\nabla}. \tag{2.6}$$

Here we obtain the relationship between the vector potential and the electric field in the absence of the electric current by using $\boldsymbol{B} = \nabla \times \boldsymbol{A}$ and the Maxwell equation for current density $\boldsymbol{j} = 0$ in vacuum, $\nabla \times \boldsymbol{B} = \mu_0\varepsilon_0 \frac{\partial \boldsymbol{E}}{\partial t}$, as follows:

$$\begin{aligned} \nabla \times \nabla \times \boldsymbol{A} = \nabla(\nabla \cdot \boldsymbol{A}) - \nabla^2 \boldsymbol{A} = \mu_0\varepsilon_0 \frac{\partial \boldsymbol{E}}{\partial t}, \\ \nabla^2 \boldsymbol{A} = \mu_0\varepsilon_0 \frac{\partial \boldsymbol{E}}{\partial t} \end{aligned} \tag{2.7}$$

The electric field of light can be described by $\boldsymbol{E} = E_0 \exp\{i(\boldsymbol{k}_{opt} \cdot \boldsymbol{r} - \omega t)\}\boldsymbol{P}$, where $\boldsymbol{P}$ is the unit vector in the direction of electric field and $\boldsymbol{k}_{opt}$ denotes the wavenumber of light. Then, we calculate the vector potential for the electric field by solving the differential equation Eq. (2.7). Using the relation $\omega = ck_{opt}$, $c = 1/\sqrt{\varepsilon_0\mu_0}$, the laser intensity $I_0 = E_0^2/\mu_0 c$, and $\nabla \cdot \boldsymbol{A} = 0$, where ω, ε_0 and ν_0 are the frequency of the light, vacuum permittivity, and vacuum permeability, respectively, the vector potential $\boldsymbol{A}$ is written as:

$$\boldsymbol{A} = \frac{i}{\omega}\sqrt{\frac{I_0}{c\varepsilon_0}} \exp\{i(\boldsymbol{k}_{opt} \cdot \boldsymbol{r} - \omega t)\}\boldsymbol{P}. \tag{2.8}$$

Using Eqs. (2.6), we obtain the electron-photon matrix element

$$\begin{aligned} M_{opt}^{fi} &= \langle f|H_{opt}|i\rangle \\ &= -\frac{ie\hbar}{m}\langle f|\boldsymbol{A} \cdot \nabla|i\rangle, \end{aligned} \tag{2.9}$$

where i and f denote the initial state and the finial state, respectively. Because the wave number in the crystal is sufficiently larger than the wave number of the light ($|\boldsymbol{k}| \gg |\boldsymbol{k}_{opt}|$), we can take the vector potential $\boldsymbol{A}$ out of the integral. Then we get the electron-photon matrix element M_{opt}^{fi} as follows:

$$\begin{aligned} M_{opt}^{fi} &= \frac{e\hbar}{m\omega}\sqrt{\frac{I}{c\varepsilon_0}} \exp\{i(\omega_f - \omega_i - \omega)t\}\langle f|\nabla|i\rangle \cdot \boldsymbol{P} \\ &= \frac{e\hbar}{m\omega}\sqrt{\frac{I}{c\varepsilon_0}} \exp\{i(\omega_f - \omega_i - \omega)t\}\boldsymbol{D}^{fi} \cdot \boldsymbol{P}, \end{aligned} \tag{2.10}$$

where the dipole vector $\boldsymbol{D}^{fi}$ is defined as

$$\boldsymbol{D}^{fi} = \langle f|\nabla|i\rangle. \tag{2.11}$$

Once we obtain the wave function of electrons, we can calculate the dipole vector $\boldsymbol{D}^{fi}$ and further the electron-photon matrix element. We use Quantum Espresso [22], where the wave function of an electron $\Psi^n(\boldsymbol{r}, \boldsymbol{k})$ is expanded by the basis set of plane wave as follows:

$$\Psi^n(\boldsymbol{r}, \boldsymbol{k}) = \sum_{\boldsymbol{G}} C_{\boldsymbol{G}}^n(\boldsymbol{k}) \exp\{i(\boldsymbol{k} + \boldsymbol{G})\boldsymbol{r}\}, \tag{2.12}$$

where $\boldsymbol{G}$ is the reciprocal lattice vector and $C_{\boldsymbol{G}}^n(\boldsymbol{k})$ is the coefficient for plane wave basis with the wave number $\boldsymbol{k} + \boldsymbol{G}$. The accuracy of the wave function $\Psi^n(\boldsymbol{r}, \boldsymbol{k})$ increases with increasing number of the reciprocal lattice vector $\boldsymbol{G}$, and we can control the number of $\boldsymbol{G}$ by the energy-cutoff parameter in Quantum Espresso. Substituting the wave function in Eq. (2.12) into Eq. (2.11), the $\boldsymbol{D}^{fi}(\boldsymbol{k})$ is expanded as follows:

$$\begin{aligned}\boldsymbol{D}^{fi}(\boldsymbol{k}) &= i\sum_{\boldsymbol{G}}\sum_{\boldsymbol{G'}} C^{f}_{\boldsymbol{G'}}(\boldsymbol{k})^{*} C^{i}_{\boldsymbol{G}}(\boldsymbol{k})(\boldsymbol{k}+\boldsymbol{G})\int \exp\{i(\boldsymbol{G}-\boldsymbol{G'})\boldsymbol{r}\}d\boldsymbol{r} \\ &= i\sum_{\boldsymbol{G}}\sum_{\boldsymbol{G'}} C^{f}_{\boldsymbol{G'}}(\boldsymbol{k})^{*} C^{i}_{\boldsymbol{G}}(\boldsymbol{k})(\boldsymbol{k}+\boldsymbol{G})\delta_{\boldsymbol{G},\boldsymbol{G'}} \\ &= i\sum_{\boldsymbol{G}} C^{f}_{\boldsymbol{G}}(\boldsymbol{k})^{*} C^{i}_{\boldsymbol{G}}(\boldsymbol{k})(\boldsymbol{k}+\boldsymbol{G}). \end{aligned} \tag{2.13}$$

2.2.2 Steps of the calculation for the electron-photon dipole vectors

In order to calculate the electron-photon dipole vector, we need to calculate the eigen values and eigen vectors by Quantum Espresso. We show the commands in Table.2.1. pw.x and pw_export.x are executable files in Quantum espresso. tap.scf.in, tap.nscf.in and pw_export.in are input files for TaP that include the parameters used in the programs. tap.scf.out, tap.nscf.out, pw_export.out are output files where we can read the results and logs of the calculation. In step 1, the self- consistent calculation is done, and the eigen values and eigen vectors are calculated for small number of k-points in reciprocal space. Then, we increase the number of k-points in non self-consistent calculation to obtain sufficient density of the eigen values and eigen vectors. In step 3, we transfer the file that consists the eigen values and eigen vectors into xml format to be used in next step.

Table 2.1: Commands for calculating electron-photon interaction.

step	Command
1	pw.x < tap.scf.in > tap.scf.out
2	pw.x < tap.nscf.in > tap.nscf.out
3	pw_export.x < pw_export.in > pw_export.out

For any laser energy, we can calculate the electron-photon dipole vectors by our own program Raman. Commands are shown in Table 2.2. It is important to note that above command not only calculates the electron-photon dipole vectors but also combines with electron-phonon interaction elements to calculate final Raman tensor. Thus, this command is used after we obtain the electron-phonon interaction elements.

Table 2.2: Commands for calculating Raman intensity.

step	Command
1	raman.x < raman.in > raman.out

2.3 Electron-phonon interaction

2.3.1 The derivation of the electron-phonon interaction

As we know the atoms in a crystal oscillate around the equilibrium position. Atomic vibration modifies the potential in the crystal that is a perturbation of the energy of an electron. We called such a interaction between the electrons and the atomic vibration as electron-phonon interaction. When the ion shifts $\boldsymbol{u}_s$ from the equilibrium position $\boldsymbol{R}_{s0}$, the atomic potential $V(\boldsymbol{r}-\boldsymbol{R}_s)$ is expended by $\boldsymbol{u}_s$ as follows:

$$\begin{aligned}
V(\boldsymbol{r}-\boldsymbol{R}_s) &= V(\boldsymbol{r}-\boldsymbol{R}_{s0}-\boldsymbol{u}_s) \\
&= V(\boldsymbol{r}-\boldsymbol{R}_{s0}) + \boldsymbol{u}_s \cdot \nabla_{\boldsymbol{u}_s} V(\boldsymbol{r}-\boldsymbol{R}_{s0}-\boldsymbol{u}_s)|_{\boldsymbol{u}_s=0} \\
&= V(\boldsymbol{r}-\boldsymbol{R}_{s0}) + \boldsymbol{u}_s \cdot \nabla_{\boldsymbol{R}_s} V(\boldsymbol{r}-\boldsymbol{R}_s)|_{\boldsymbol{R}_s=\boldsymbol{R}_{s0}}, \qquad (2.14)
\end{aligned}$$

where we consider the displacement $\boldsymbol{u}_s$ as a perturbation. The first term in Eq. (2.14) is an unperturbed potential used in the electronic band structure calculation while the second term gives electron-phonon interaction. Here we derive the matrix element of the electron-phonon interaction for the process that the electron moves from the initial state (i) to the final state (f) by emitting a $\boldsymbol{q}=0$ phonon in the first-order Raman process as follows:

$$\begin{aligned}
M_{ep}^{fi\nu}(\boldsymbol{k},\boldsymbol{k}) &= \sum_s \sqrt{\frac{\hbar}{2M_s\omega_\nu}} \langle \psi^f(\boldsymbol{k},\boldsymbol{r})|\boldsymbol{u}_s \cdot \nabla_{\boldsymbol{R}_s} V(\boldsymbol{r}-\boldsymbol{R}_s)|_{\boldsymbol{R}_s=\boldsymbol{R}_{s0}}|\psi^i(\boldsymbol{k},\boldsymbol{r})\rangle \\
&= \sum_s \sqrt{\frac{\hbar}{2M_s\omega_\nu}} \boldsymbol{u}_s \cdot D_{ep}^{fi}(\boldsymbol{k}), \qquad (2.15)
\end{aligned}$$

where $D_{ep}^{fi}(\boldsymbol{k})$ is defined as $\langle \psi^f(\boldsymbol{k},\boldsymbol{r})|\nabla_{\boldsymbol{R}_s} V(\boldsymbol{r}-\boldsymbol{R}_s)|_{\boldsymbol{R}_s=\boldsymbol{R}_{s0}}|\psi^i(\boldsymbol{k},\boldsymbol{r})\rangle$ and M_s, ω_ν are the mass of the ion labeled by s, the frequency of the phonon, respectively. According to the conservation of momentum, $\boldsymbol{q}=0$ phonon does not change the wave number of the electron and thus the wave number is k for both the initial state (i) and the final state (f). In this work, we calculate the phonon and the electron wave function by using Quantum Espresso [22]. Then, we calculate the electron-phonon interaction using EPW package [23]. EPW uses the Wannier function as basis functions rather than the plane wave functions in Quantum Espresso, which are convenient to represent phonon perturbation localized in real space.

The relation between the Bloch functions $\psi^n(\boldsymbol{r},\boldsymbol{k})$ and the Wannier functions $w^m(\boldsymbol{r},\boldsymbol{R_e})$ is given by a Fourier transform in the momentum k and lattice vector R_e variables as follows:

$$\Psi^n(\boldsymbol{r},\boldsymbol{k}) = \frac{1}{N_e} \sum_{m\boldsymbol{R}_e} U^\dagger_{mn,\boldsymbol{k}} \exp\{i\boldsymbol{k}(\boldsymbol{r}-\boldsymbol{R}_e)\} w^m(\boldsymbol{r},\boldsymbol{R}_e), \qquad (2.16)$$

where is N_e the number of unit cells in the supercell, corresponding to the number of k points included in the calculation. R_e is the position of the unit cell, and $U^\dagger_{\boldsymbol{mn},k}$ is the coefficient of the Fourier transform. The phonon perturbation for phonon mode ν and the momentum q in the Wannier representation is expressed as follows:

$$\nabla^{\nu,\boldsymbol{q}}_{\boldsymbol{R}_s} V(\boldsymbol{r}-\boldsymbol{R}_s) = \sum_{s\boldsymbol{R}_p} u^{\nu}_{\boldsymbol{q},s} \exp\{i\boldsymbol{q}(\boldsymbol{r}-\boldsymbol{R}_p)\}\nabla_{s,\boldsymbol{R}_p} V(\boldsymbol{r}-\boldsymbol{R}_s), \tag{2.17}$$

where $u^{\nu}_{\boldsymbol{q},s}$ is displacement field. R_p is the position of the unit cell and s notes the ion in the unit cell. In our calculation, the momentum $q = 0$. By substituting Eq. (2.16) and Eq. (2.17) into Eq. (2.15), we obtain the electron-phonon interaction dipole vectors in Wannier representation as follows:

$$\begin{aligned} D^{fi}_{ep}(\boldsymbol{k}) &= \frac{1}{{N_e}^2} \sum_{m,n,\nu} \sum_{\boldsymbol{R}_e,\boldsymbol{R}_e{}',\boldsymbol{R}_p} \exp\{i\boldsymbol{k}(\boldsymbol{R}_e-\boldsymbol{R}_e{}')\} u^{\nu}_{\boldsymbol{q},s} U_{fm,\boldsymbol{k}} \\ & \quad \dot{U}^{\dagger}_{in,\boldsymbol{k}} \int w^m(\boldsymbol{r},\boldsymbol{R}_e{}')^* \nabla_{s,\boldsymbol{R}_p} V(\boldsymbol{r}-\boldsymbol{R}_s) w^n(\boldsymbol{r},\boldsymbol{R}_e) d\boldsymbol{r}, \end{aligned} \tag{2.18}$$

where n (m) notes the Wannier band for initial (final) state i (f), and $\boldsymbol{R}_e$ ($\boldsymbol{R}_e{}'$) notes the position of the unit cell for initial (final) state i(f). $U_{fm,\boldsymbol{k}}$ ($U^{\dagger}_{in,\boldsymbol{k}}$) is arbitrary unitary rotation operator for k point. EPW package will minimize the localization function $\Omega = \sum_m \int (w^m(\boldsymbol{r},0)^* w^m(\boldsymbol{r},0)\boldsymbol{r^2} - (w^m(\boldsymbol{r},0)^* w^m(\boldsymbol{r},0)\boldsymbol{r})^2) d\boldsymbol{r}$ with respect all the sets of unitary transformation.

2.3.2 Steps of the calculation for the electron-phonon interaction elements

First, we need to calculate the eigen values and eigen vectors for phonons by Quantum Espresso. The commands is shown in Table 2.3. The self-consistent calculation is done in step 1. Then, the eigen values and eigen vectors for phonons are calculated in step 2.

Table 2.3: Commands for calculating Γ point phonon.

step	Command
1	pw.x < tap.scf.in > tap.scf.out
2	pw.x < tap.ph.in > tap.ph.out

Second, we calculate the electro-phonon interaction elements by using EPW package. The commands are shown in Table 2.4. In step 1, the self-consistent calculation

Table 2.4: Commands for calculating electron-phonon interaction.

step	Command
1	pw.x < tap.scf.in > tap.scf.out
2	pw.x < tap.nscf.in > tap.nscf.out
3	epw.x < epw.in > epw.out

is done. Then, we increase the number of k-points in non self-consistent calculation to obtain sufficient density of the eigen values and eigen vectors for the electron. Here the k-points in reciprocal space should be same as the k-points in the calculation for the electron-photon dipole vector. Finally, the electron-phonon interaction elements are calculated by epw.x. For the finial step, EPW package first reads the wavefunctions in the Bloch representation from Quantum Espresso. Then, it calculate the overlap matrices and projection matrices. Finally, it minimizes the localization function and calculates the electron-phonon interaction by Wannier functions.

Chapter 3

Laser energy dependence of polarized Raman spectra for TaP

In this chapter, we discuss the origin of two main unique features beyond the resonant Raman theory in the measured Polarized Raman spectra of TaP as shown in the section 1.3.3. First, the polar plot of Raman intensity show systematic deviation from the prediction of the Raman tensor theory. Second, the B_1^1 mode is absent for the 633 nm excitation.

3.1 Electronic and phonon energy dispersion of TaP

TaP belongs to body-centered tetragonal space group $I4_1md$ (No. 109, C_{4v}) as shown in Fig. 1.6. The reciprocal lattice of TaP is shown in Fig. 3.1(a), illustrating the high symmetry points of the Brillouin zone (Γ, Σ, S, Z, N, X). In Figs. 3.1(b) and (c), we show the calculated electronic band structures of TaP without and with spin-orbit coupling (SOC), respectively, along high symmetry paths of the Brillouin zone (Γ-Σ-S, Fig. 3.1(a)), consistent with the previous calculations [24]. Since there are two Ta and two P atoms in the primitive unit cell of TaP, it has twelve phonon modes in which four modes are doubly degenerate E modes. Vibrational modes of TaP consist of three acoustic phonon modes [A_1 + E] and nine optical phonon modes [A_1 + $2B_1$ + 3E], and we show the energy dispersion of these vibrational modes in Fig. 3.2

Fig. 3.1: Fig/ch3-elebnd.pdf
Fig. 3.2: Fig/ch3-phonon.pdf

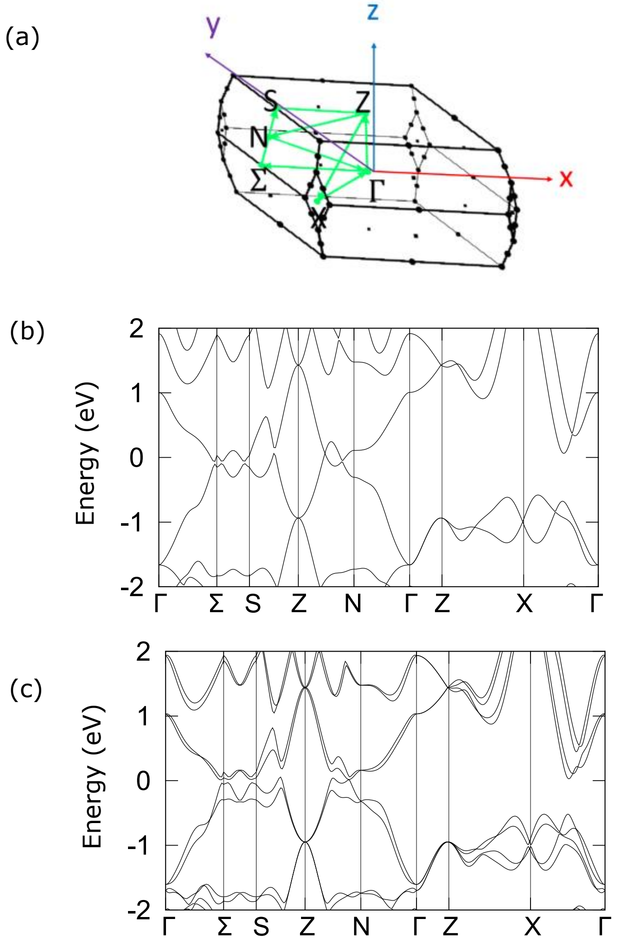

Figure 3.1 Calculated energy band structure of TaP. (a) Schematics of the high symmetry lines in the Brillouin zone considered for the DFT calculations. (b) Calculated energy band structure without SOC and (c) with SOC using DFT

3.2 Calculated polarized Raman spectra by first principles calculation

In this section, we performed first-principles DFT calculations for the polarization dependence of Raman intensity with five different excitation wavelengths that match the experimental values including 366, 492, 536, 639, 794 nm. Here the laser wavelengths in the calculation are slightly shifted from the laser wavelengths used in the experiment that are 364, 488, 532, 633, 785 nm. Such a shift is necessary to offset the difference between the calculated electronic energy dispersion and the measurement in experiment. On the one hand, the DFT calculations as shown in Fig. 3.3(b)

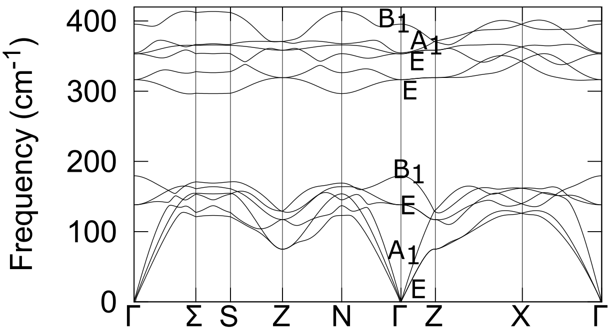

Figure 3.2 Calculated energy dispersion of the phonon modes in TaP. TaP has three acoustic phonon modes [A_1 + E] and nine optical phonon modes [A_1 + $2\mathrm{B}_1$ + 3E].

can reproduce several features in the experiments as shown in Fig. 3.3(a). First, the calculated Raman spectra of B_1^1 mode for 639 nm excitation shows a sufficient small value that is consistent with signal disappearance of B_1^1 mode for 633 nm excitation in experiment. Second, in the calculation, the angular dependences of the A_1 mode for 492 and 536 nm excitations are highly isotropic but those for the other three laser excitations are slightly anisotropic. Similar features of the A_1 mode are observed in the measurement including the circular-shaped polar plots for 488 and 532 nm excitations and the elliptical-shaped polar plots for 364, 633, 785 nm excitations. Furthermore, the calculations show a non-four-fold symmetry of the B_1^2 modes consistent with measurements. For example, the calculated B_1^2 mode for 536 nm excitation has the second maximal at the polarization angle $\theta = 180°$, same as the measured one for 532 nm excitation. On the other hand, there are some discrepancies between experiments and DFT calculations. For instance, the second maximal of the calculated B_1^2 mode for 639 nm excitation are rotated by 90 with respect to the measured result for 633 nm excitation. Moreover, the calculated relative Raman intensity of the A_1 mode is overestimated by one order of magnitude. Those discrepancies can be explained by adopting an adjustable parameter of γ as explained in next section.

3.3 The origin of the asymmetry of the polarized Raman spectroscopy

In this section, we explain the non-four-fold symmetry of the B_1^2 modes and the anisotropic symmetry for the A_1 mode by resonance window line-width γ. In Eq. (2.1), there are two energy denominators: $E_\mathrm{L} - E^{mi} - i\gamma$ and $E_\mathrm{L} - E^{m'i} \pm \hbar\omega_\nu - i\gamma$. When the resonance effect occurs, which means the values of $E_\mathrm{L} - E^{mi}$ or $E_\mathrm{L} - E^{m'i} \pm \hbar\omega_\nu$

Fig. 3.3: Fig/ch3-calcu.pdf
Fig. 3.4: Fig/ch3-2cases.pdf
Fig. 3.5: Fig/ch3-gamma.pdf
Fig. 3.6: Fig/ch3-mm'.pdf

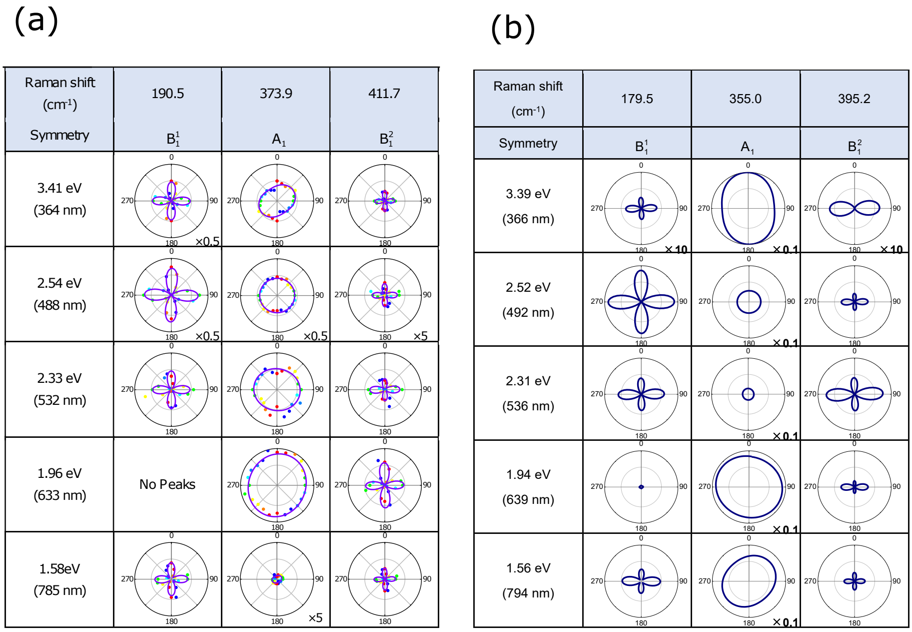

Figure 3.3 (a) Experimental polar plot of Raman intensity for TaP. (b) Calculated polar plot of Raman intensity for TaP that consists of the B_1^1, A_1 and B_1^2 modes for five laser excitations including 366, 492, 536, 639, 794 nm. The peak disappearance of B_1^1 mode for 639 nm excitation is reproduced in the calculation. The non-four-fold symmetry for B_1 mode and the anisotropic symmetry for A_1 mode appear in both experimental results and the calculated results.

are near 0, the Raman intensity strongly depends on the broadening factor γ. In other words, the intermediate states of the first-order Raman scattering processes will be changed when we choose different γ values. For TaP, since the conduction bands are degenerate at some specific k-points in the Brillouin zone (Fig. 3.5(a)), we can consider two cases. One is that the γ value is comparable to the energy difference between two degenerate conduction bands as shown in Fig. 3.4(a), then both conduction bands can be chosen as the intermediate state. Therefore, both of them contribute to the Raman intensity and the interference between two conduction bands also influences the Raman intensity. The other one is that the γ value is much smaller than the energy difference between two non-degenerate conduction bands as shown in Fig. 3.4(b), only one conduction band can be chosen as the intermediate state and mainly contributes to the Raman intensity. Thus, the interference between two conduction bands would not occur. In Fig 3.5(b), we show the calculated polarization dependence for two different γ values of 0.1 eV and 0.01 eV at the laser excitation of 2.52 eV (492 nm) and 1.94 eV (639 nm) for the B_1^2 Raman shift of 395.2 cm^{-1}. We find that when γ is 0.01 eV, which is much smaller than the energy difference between the degenerate bands, the four-fold symmetry for B_1 mode is remained as the Raman tensor the-

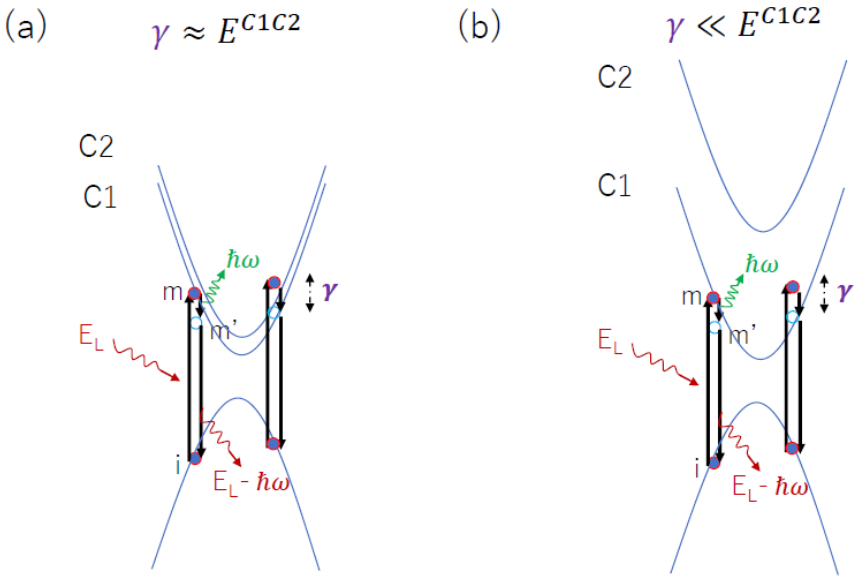

Figure 3.4 The interference between two conduction bands. (a) There is interference between two degenerate conduction bands. When E^{C1C2} that is the energy difference between two bands C1 and C2, is comparable with the γ, C1 and C2 both can be chosen as the intermediate state $m^{'}$. (b) there is no interference between non-degenerate bands. When E^{C1C2} is much larger than the γ value, only C1 can be chosen as the intermediate state.

ory predicts. However, when γ is 0.1 eV that is comparable to the energy difference between degenerate bands, the non four-fold symmetry reproduces the experimental polar plot of the Raman intensity. Since $\gamma = \frac{\hbar}{2\tau}$ is related to the inverse of the lifetime of photo-excited electron τ, the γ values depend on the laser energy. Therefore, the anisotropic behavior of the A_1 mode and the non-four-fold symmetry of the B_1 mode only appear at specific laser wavelength excitation, which is consistent with the experiments (see Fig. 1.8). In order to show the roles that quantum interference plays, we artificially remove the quantum interference effect in the calculation. That is, we calculate Raman intensity in which we intentionally select the cases of $m' = m$ in the summation of m' in Eq. (2.1) in the computational program. In this case, the deviation of the polarized Raman spectra does not happen for all phonon modes and for all laser energies as shown in Fig. 3.6. Thus, the deviation occurs as the quantum interference effect when the contribution of $m' \neq m$ to Raman scattering amplitude is not negligible.

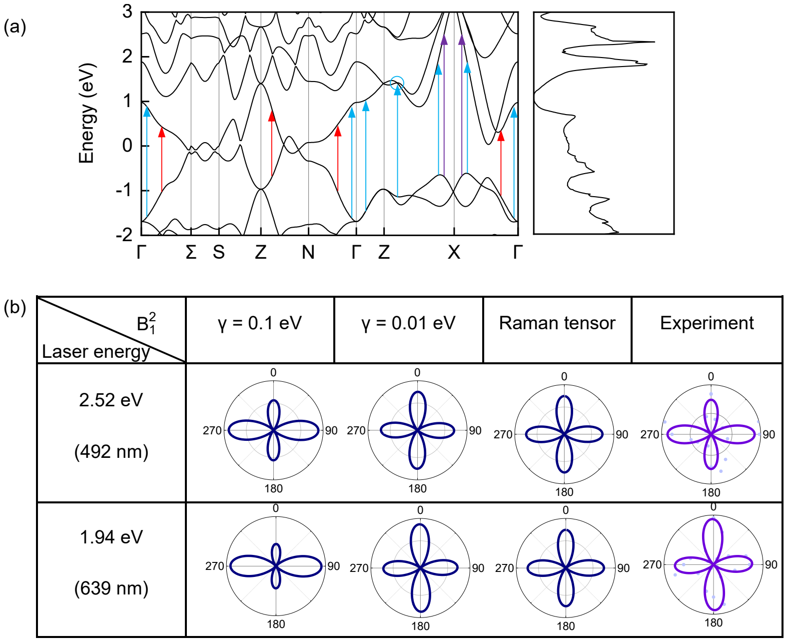

Figure 3.5 γ value dependence of TaP. (a) Excitations for 1.56 (red arrows), 2.52 (blue arrows), and 3.39 eV (purple arrows). For 2.52 eV, the conduction bands circled are degenerate. The right panel is the density of states. (b) Calculated polar plot of the Raman intensity for two γ values of 0.1 eV and 0.01 eV. For comparison, we also show the polar plot of classical Raman tensor theory and the experiment for 2.52 and 1.94 eV laser excitation. The intensity scales of the polar plots are adjusted for clearer view.

3.4 The origin of the disappearance of Raman intensity

Both in the calculations (see Fig. 3.3) and the experiments (see Fig. 1.8), the Raman spectra of B_1^1 mode is absent for 633 nm (1.94 eV) excitation. To explain the absence of the B_1^1 mode for laser energy $E_L = 1.96$ eV, we calculate the polarized Raman spectra of the B_1^1 mode for excitations of 1.91-1.97 eV as shown in Fig. 3.7. In our calculation, the Raman intensity changes as the function of laser energy of excitation. The Raman intensity decreases when the laser energy of excitations increase from 1.91 eV to 1.94 eV, while it increases as the laser energy of excitations increase from 1.94 eV to 1.97 eV. Because when the laser energy changes, the initial state (finial state), immediate state, that satisfy the resonance conditions $E_\mathrm{L} = E^{mi}$ or $E_\mathrm{L} = E^{m'i} \pm \hbar\omega_\nu$, also change, and thus the corresponding electron-photon, electron-phonon matrix element change. The Raman intensity has a minimum at $E_L = 1.94$ eV that is consistent with the experimental results after considering of the energy shift in DFT calculation. The reason why the B_1^1 mode become absent is that the interference effect of Raman scattering amplitude cancels the Raman intensity. In fact, if we select one of the degenerate band as the intermediate state, we get a finite Raman intensity.

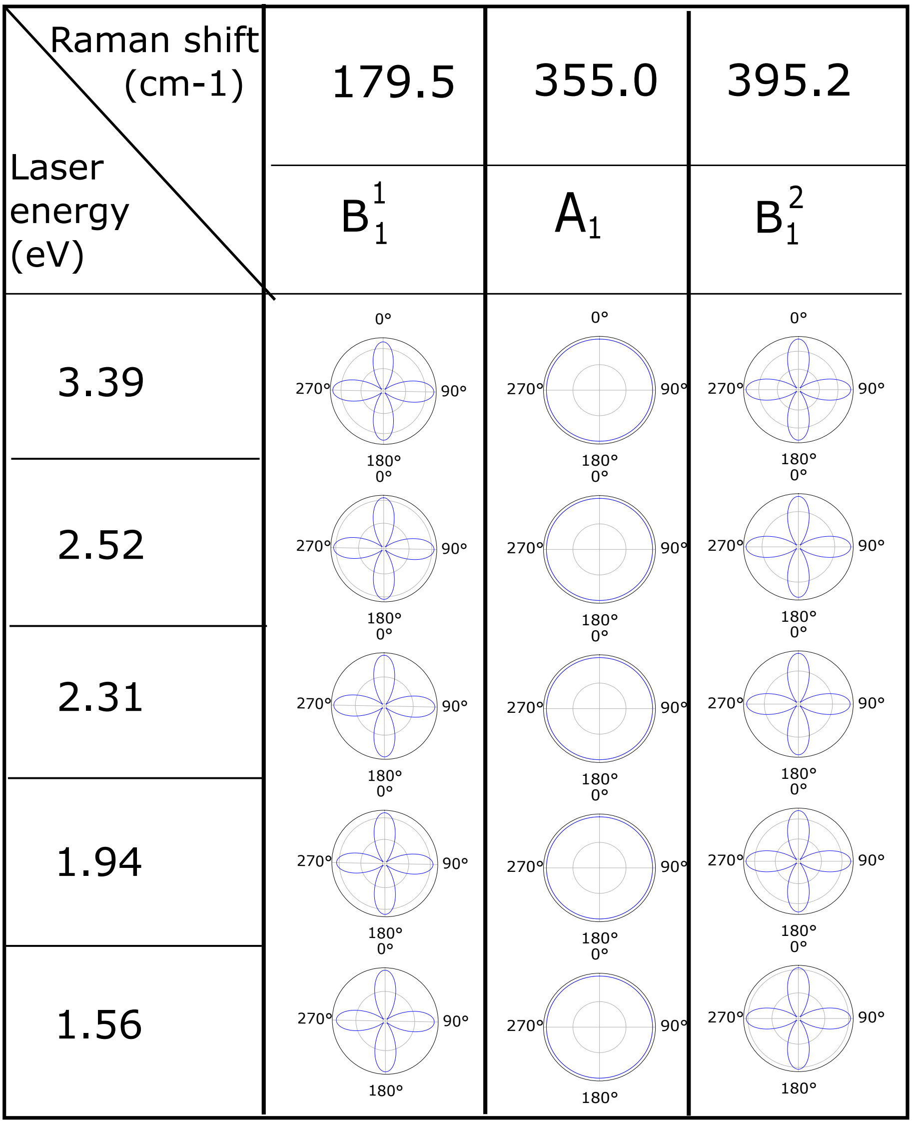

Figure 3.6 The calculated polar plot of the Raman intensity of the B$_1^1$, A$_1$, B$_1^2$ modes do not show any deviation from the symmetry of phonons when we intentionally select $(m\ m')$ = (C1, C1), and (C2, C2) in Eq. (2.1) in the resonant Raman intensity calculation.

Fig. 3.7: Fig/ch3-absence.pdf

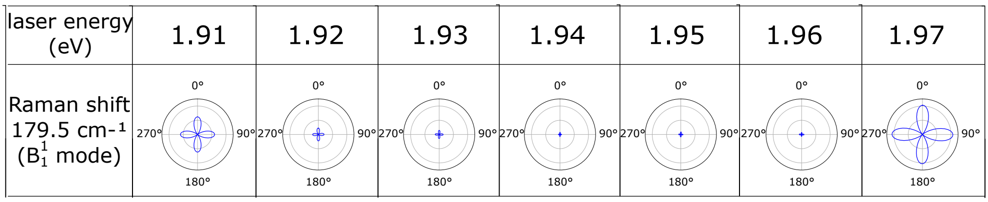

Figure 3.7 The calculated polar plot of the Raman intensity of the B_1^1 for excitations of 1.91-1.97 eV.

Chapter 4

Conclusions

To explain the asymmetry in the polar plot of the Raman intensity, and spectra absence of the B_1^1 mode for laser energy $E_L = 1.96$ eV in experimental result, we performed the theoretical analysis accompanied with first-principles calculation. We employ Quantum Espresso [22] to obtain the eigen values and eigen vectors of electrons and phonons in TaP. Further using EPW package [23], we calculate the electron-phonon interaction. Finally, we calculate the electron-photon interaction and the first-order resonant Raman intensity by our homemade program, where the broadening factor γ is adapted as a parameter. By adjusting the broadening factor γ in the resonant Raman intensity, we reproduce and explain the unique features of the polarized Raman spectra for TaP in experiments. First, the non-four-fold symmetry of the B_1^2 modes and the anisotropic symmetry for the A_1 mode is caused by quantum interference between degenerate conduction bands. Because when γ is much smaller than the energy difference between degenerate bands, which means the interference between degenerate bands are ignorablethe asymmetries disappear. Moreover, the asymmetries also disappear, if we avoid the interference by selecting only one conduction band as the intermediate state. Second, the origin of the absence of the B_1^1 mode for 1.96 eV laser energy excitation is that the interference effect of Raman scattering amplitude cancels the Raman intensity. In calculation, the Raman intensity has a minimum at $E_L = 1.94$ eV that is consistent with the experimental results after considering of the energy shift in DFT calculation.

Appendix A

Details of numerical calculations

Here we show details of the parameters used in numerical calculations in Chapter 3.

DFT calculations: The calculations of Raman intensity in TaP are based on DFT based first-principles calculations. First, we use the QuantumESPRESSO package [22] to obtain the electronic structure and phonon dispersion of TaP. Here, the potentials between ionic cores and valence electrons are modeled with norm-conserving pseudopotentials. The X-C energy of electrons is approximated within a local density approximation (LDA) [25]. The cutoff energy 150 Ry is adopted to achieve the convergence of total energy. Using the calculated wavefunctions, we obtain the electron-photon matrix element by the home-made program [26]. Further, we use the electron-phonon Wannier package [23] to calculate the electron-phonon matrix elements for the phonon wavevector at the Γ point in the Brillouin zone. In the calculations, the lattice parameters of TaP are optimized to $a = 0.33363$ nm, $c = 1.14077$ nm by the geometrical optimization, and the resonance window line-width γ is adopted as an adjustable parameter.

Appendix B

The derivation of the Raman intensity formula

In this section, we use the time-dependent perturbation theory to derive the Raman scattering formula. The Raman spectra is described by the interaction between the light and the material. Since light is an electromagnetic wave, Raman scattering can be considered as a time-dependent perturbation added to the original system of the material.

B.1 General time-dependent perturbation Hamiltonian

We write the Hamiltonian as,

$$H(t) = H_0 + H'(t), \tag{B.1}$$

where $H'(t)$ is the time-dependent perturbation and the H_0 is the time-independent unperturbed Hamiltonian. The time-dependent eigen state $|\Psi(t)\rangle$ satisfies the time-dependent Schrödinger equation as follows:

$$i\hbar\frac{\partial}{\partial t}|\Psi(t)\rangle = H(t)|\Psi(t)\rangle. \tag{B.2}$$

We define the eigen state $|m\rangle$ with the eigen energy E_m for unperturbed Hamiltonian H_0 that is the Hermitian operator.

$$H_0|m\rangle = E_m|m\rangle. \tag{B.3}$$

The eigen states of Hamiltonian H_0 form a complete orthonormal set that can be expressed as follows:

$$\langle n|m\rangle = \delta_{nm}, \tag{B.4}$$

$$\sum_m |m\rangle\langle m| = 1, \tag{B.5}$$

where δ_{nm} denotes the Kronecker delat ($\delta_{nm} = 1$ for $n = m$, otherwise 0). The time-dependent eigen state $|\Psi(t)\rangle$ can be expressed by the orthonormal complete set as follows:

$$|\Psi(t)\rangle = \sum_m a_m(t) e^{\frac{E_m}{i\hbar}t} |m\rangle, \tag{B.6}$$

where $a_m(t)$ is the time-dependent expansion coefficient. Substituting Eq. (B.6) into (B.2), we obtain the right- and left-hand sides of Eq. (B.2) respectively as follows:

$$\begin{aligned} i\hbar \frac{\partial}{\partial t}|\Psi(t)\rangle &= \sum_m \left\{ i\hbar \frac{\partial a_m(t)}{\partial t} + E_m a_m(t) \right\} e^{\frac{E_m}{i\hbar}t}|m\rangle, & \text{(B.7)} \\ H(t)|\Psi(t)\rangle &= (H_0 + H'(t))|\Psi(t)\rangle & \text{(B.8)} \\ &= \sum_m (E_m + H'(t)) a_m(t) e^{\frac{E_m}{i\hbar}t}|m\rangle. & \text{(B.9)} \end{aligned}$$

With the right-hand side equaling to the left-hand side of Eq. (B.2), we obtain

$$i\hbar \sum_m \frac{\partial a_m(t)}{\partial t} e^{\frac{E_m}{i\hbar}t}|m\rangle = \sum_m H'(t) a_m(t) e^{\frac{E_m}{i\hbar}t}|m\rangle. \tag{B.10}$$

By multiplying $\sum_{m'} |m'\rangle\langle m'|$ that equals to 1 to the both sides of Eq. (B.10), we obtain

$$\sum_{m'} \left\{ i\hbar \frac{\partial a_{m'}(t)}{\partial t} e^{\frac{E_{m'}}{i\hbar}t} - \sum_m a_m(t) e^{\frac{E_m}{i\hbar}t} \langle m'|H'(t)|m\rangle \right\} |m'\rangle = 0. \tag{B.11}$$

By multiplying $\langle n|$ from the left side of Eq. (B.11), we obtain

$$\frac{\partial a_n(t)}{\partial t} = \frac{1}{i\hbar} \sum_m a_m(t) e^{\frac{E_m - E_n}{i\hbar}t} \langle n|H'(t)|m\rangle. \tag{B.12}$$

By integrating Eq. (B.12) from t_0 to t, we obtain the time-dependent coefficient $a_n(t)$ as follows:

$$a_n(t) = a_n(t_0) + \frac{1}{i\hbar} \sum_m \int_{t_0}^{t} dt' a_m(t) e^{\frac{E_m - E_n}{i\hbar}t} \langle n|H'(t')|m\rangle. \tag{B.13}$$

In Eq. (B.13), substituting the left-hand side to right-hand side iteratively, we obtain the expression of $a_n(t)$ as follows:

$$\begin{aligned}
a_n(t) \quad = \quad & a_n(t_0) + \frac{1}{i\hbar}\sum_m \int_{t_0}^{t} dt' a_m(t_0) e^{\frac{E_m - E_n}{i\hbar}t'} \langle n|H'(t')|m\rangle \\
& + \frac{1}{(i\hbar)^2}\sum_m \sum_{m'} \int_{t_0}^{t} dt' \int_{t_0}^{t'} dt'' a_{m'}(t_0) e^{\frac{E_{m'} - E_m}{i\hbar}t} e^{\frac{E_m - E_n}{i\hbar}t} \\
& \times \langle n|H'(t')|m\rangle \langle m|H'(t'')|m'\rangle \\
& + \frac{1}{(i\hbar)^3}\sum_m \sum_{m'} \sum_{m''} \int_{t_0}^{t} dt' \int_{t_0}^{t'} dt'' \int_{t_0}^{t''} dt''' a_{m''}(t_0) e^{\frac{E_{m''} - E_{m'}}{i\hbar}t} e^{\frac{E_{m'} - E_m}{i\hbar}t} \\
& \times e^{\frac{E_m - E_n}{i\hbar}t} \langle n|H'(t')|m\rangle \langle m|H'(t'')|m'\rangle \langle m'|H'(t''')|m''\rangle \\
& + \ldots.
\end{aligned} \tag{B.14}$$

where the $a_n(t_0)$ must satisfy the initial condition as follows:

$$|\Psi(t_0)\rangle = \sum_n a_n(t_0) e^{\frac{E_n}{i\hbar}t_0} |n\rangle = |i\rangle. \tag{B.15}$$

The solution of $a_n(t_0)$ is expressed by

$$a_n(t_0) = \delta_{ni}. \tag{B.16}$$

The first-, second-, and third-order perturbation coefficients noted as $a_n^{(1)}(t)$, $a_n^{(2)}(t)$, and $a_n^{(3)}(t)$ are the second, third, and fourth terms in Eq. (B.14) respectively. They can be further written as

$$a_n^{(1)}(t) \quad = \quad \frac{1}{i\hbar}\int_{t_0}^{t} dt' e^{\frac{E_i - E_n}{i\hbar}t'} \langle n|H'(t')|i\rangle, \tag{B.17}$$

$$a_n^{(2)}(t) \quad = \quad \frac{1}{(i\hbar)^2}\sum_m \int_{t_0}^{t} dt' \int_{t_0}^{t'} dt'' e^{\frac{E_i - E_m}{i\hbar}t''} e^{\frac{E_m - E_n}{i\hbar}t'} \langle n|H'(t')|m\rangle \langle m|H'(t'')|i\rangle, \tag{B.18}$$

$$\begin{aligned}
a_n^{(3)}(t) \quad = \quad & \frac{1}{(i\hbar)^3}\sum_m \sum_{m'} \int_{t_0}^{t} dt' \int_{t_0}^{t'} dt'' \int_{t_0}^{t''} dt''' e^{\frac{E_i - E_{m'}}{i\hbar}t'''} e^{\frac{E_{m'} - E_m}{i\hbar}t''} e^{\frac{E_m - E_n}{i\hbar}t'} \\
& \times \langle n|H'(t')|m\rangle \langle m|H'(t'')|m'\rangle \langle m'|H'(t''')|i\rangle.
\end{aligned} \tag{B.19}$$

B.2 The Raman intensity for the first-order Raman scattering

The first-order Raman scattering process is calculated by the third-order perturbation theory. Since the perturbation here is light (electromagnetic wave), we define the perturbation Hamiltonian as

$$H'(t) = e^{\eta_1 t} V_1 e^{\pm i\omega_1 t} + e^{\eta_2 t} V_2 e^{\pm i\omega_2 t} + e^{\eta_3 t} V_3 e^{\pm i\omega_2 t} ..., \tag{B.20}$$

where η_1 and η_2 are the factors of the potential decay. Substituting the perturbation Hamiltonian in Eq. (B.20) into the third-order perturbation coefficient $a_n^{(3)}(t)$ in Eq. (B.19), we obtain

$$
\begin{aligned}
a_n^{(3)}(t) \quad = \quad & \frac{1}{(i\hbar)^3}\sum_m\sum_{m'}\int_{t_0}^{t}dt'\int_{t_0}^{t'}dt''\int_{t_0}^{t''}dt'''e^{\frac{i}{\hbar}(E_m-E_i\pm\hbar\omega_1-i\hbar\eta_1)t'''} \\
& \times e^{\frac{i}{\hbar}(E_{m'}-E_m\pm\hbar\omega_1-i\hbar\eta_1)t''}e^{\frac{i}{\hbar}(E_n-E_{m'}\pm\hbar\omega_1-i\hbar\eta_1)t'} \\
& \times\langle n|V_1|m'\rangle\langle m'|V_1|m\rangle\langle m|V_1|i\rangle \\
& +\frac{1}{(i\hbar)^3}\sum_m\sum_{m'}\int_{t_0}^{t}dt'\int_{t_0}^{t'}dt''\int_{t_0}^{t''}dt'''e^{\frac{i}{\hbar}(E_m-E_i\pm\hbar\omega_1-i\hbar\eta_1)t'''} \\
& \times e^{\frac{i}{\hbar}(E_{m'}-E_m\pm\hbar\omega_2-i\hbar\eta_2)t''}e^{\frac{i}{\hbar}(E_n-E_{m'}\pm\hbar\omega_3-\hbar\eta_3)t'} \\
& \times\langle n|V_3|m'\rangle\langle m'|V_2|m\rangle\langle m|V_1|i\rangle \\
& +.... \qquad \text{(B.21)}
\end{aligned}
$$

The third-order perturbation associated with V_1, V_2 and V_3, $a_{n,V_1,V_2,V_3}^{(3)}(t)$ [second term in Eq. B.21] is further calculated as follows:

$$
\begin{aligned}
a_{n,V_1,V_2,V_3}^{(3)}(t) \quad = \quad & \frac{1}{(i\hbar)^3}\sum_m\sum_{m'}\int_{t_0}^{t}dt'\int_{t_0}^{t'}dt''\int_{t_0}^{t''}dt'''e^{\frac{i}{\hbar}(E_m-E_i\pm\hbar\omega_1-i\hbar\eta_1)t'''} \\
& \times e^{\frac{i}{\hbar}(E_{m'}-E_m\pm\hbar\omega_2-i\hbar\eta_2)t''}e^{\frac{i}{\hbar}(E_n-E_{m'}\pm\hbar\omega_3-\hbar\eta_3)t'} \\
& \times\langle n|V_3|m'\rangle\langle m'|V_2|m\rangle\langle m|V_1|i\rangle \\
= \quad & \frac{1}{(i\hbar)^3}\sum_m\sum_{m'}(-i\hbar)\frac{\langle n|V_3|m'\rangle\langle m'|V_2|m\rangle\langle m|V_1|i\rangle}{E_m-E_i\pm\hbar\omega_1-i\hbar\eta_1}\int_{t_0}^{t}dt'\int_{t_0}^{t'}dt'' \\
& \left\{e^{\frac{i}{\hbar}(E_m-E_i\pm\hbar\omega_1-i\hbar\eta_1)t''}-e^{\frac{i}{\hbar}(E_m-E_i\pm\hbar\omega_1-i\hbar\eta_1)t_0}\right\} \\
& \times e^{\frac{i}{\hbar}(E_{m'}-E_m\pm\hbar\omega_2-\hbar\eta_2)t''}e^{\frac{i}{\hbar}(E_n-E_{m'}\pm\hbar\omega_3-\hbar\eta_3)t'} \qquad \text{(B.22)}
\end{aligned}
$$

After we take the limit of $t_0 \to -\infty$, the second term of Eq. (B.22) is zero. Thus, V_1, V_2 and V_3, $a^{(3)}_{n,V_1,V_2,V_3}(t)$ is further calculated as follows:

$$\begin{aligned}
a^{(3)}_{n,V_1,V_2,V_3}(t) &= \frac{1}{(i\hbar)^3}\sum_m\sum_{m'}(-i\hbar)\frac{\langle n|V_3|m'\rangle\langle m'|V_2|m\rangle\langle m|V_1|i\rangle}{E_m - E_i \pm \hbar\omega_1 - i\hbar\eta_1}\int_{-\infty}^{t} dt' \\
&\quad \times e^{\frac{i}{\hbar}(E_n - E_{m'} \pm \hbar\omega_3 - i\hbar\eta_3)t'}\int_{-\infty}^{t'} e^{\frac{i}{\hbar}(E_{m'} - E_i \pm \hbar\omega_1 \pm \hbar\omega_2 - i\hbar(\eta_1+\eta_2))t''}dt'' \\
&= \frac{1}{(i\hbar)^3}\sum_m\sum_{m'}(-i\hbar)^2 \\
&\quad \times \frac{\langle n|V_3|m'\rangle\langle m'|V_2|m\rangle\langle m|V_1|i\rangle}{(E_m - E_i \pm \hbar\omega_1 - i\hbar\eta_1)(E_{m'} - E_i \pm \hbar\omega_1 \pm \hbar\omega_2 - i\hbar(\eta_1+\eta_2))} \\
&\quad \times \int_{-\infty}^{t} dt' e^{\frac{i}{\hbar}(E_{m'} - E_i \pm \hbar\omega_1 \pm \hbar\omega_2 - i\hbar(\eta_1+\eta_2))t'} e^{\frac{i}{\hbar}(E_n - E_{m'} \pm \hbar\omega_3 - i\hbar\eta_3)t'} \\
&= \frac{1}{(i\hbar)^3}\sum_m\sum_{m'}(-i\hbar)^2 \\
&\quad \times \frac{\langle n|V_3|m'\rangle\langle m'|V_2|m\rangle\langle m|V_1|i\rangle}{(E_m - E_i \pm \hbar\omega_1 - i\hbar\eta_1)(E_{m'} - E_i \pm \hbar\omega_1 \pm \hbar\omega_2 - i\hbar(\eta_1+\eta_2))} \\
&\quad \times \int_{-\infty}^{t} dt' e^{\frac{i}{\hbar}E_n - E_i \pm \hbar\omega_1 \pm \hbar\omega_2 \pm \hbar\omega_3 - i\hbar(\eta_1+\eta_2+\eta_3))t'}
\end{aligned} \tag{B.23}$$

Then we take the limit of $t \to \infty$, $\eta_1 \to 0$ and $\eta_2 \to 0$ in the integral. We obtain

$$\begin{aligned}
a^{(3)}_{n,V_1,V_2,V_3}(t) &= \frac{1}{i\hbar}\sum_m\sum_{m'} \\
&\quad \times \frac{\langle n|V_3|m'\rangle\langle m'|V_2|m\rangle\langle m|V_1|i\rangle}{(E_m - E_i \pm \hbar\omega_1 - i\hbar\eta_1)(E_{m'} - E_i \pm \hbar\omega_1 \pm \hbar\omega_2 - i\hbar(\eta_1+\eta_2))} \\
&\quad \times \int_{-\infty}^{\infty} dt' e^{\frac{i}{\hbar}(E_n - E_i \pm \hbar\omega_1 \pm \hbar\omega_2 \pm \hbar\omega_3)t'} \\
&= 2\pi i\sum_m\sum_{m'} \\
&\quad \times \frac{\langle n|V_3|m'\rangle\langle m'|V_2|m\rangle\langle m|V_1|i\rangle}{(E_m - E_i \pm \hbar\omega_1 - i\hbar\eta_1)(E_{m'} - E_i \pm \hbar\omega_1 \pm \hbar\omega_2 - i\hbar(\eta_1+\eta_2))} \\
&\quad \times \delta\left(\frac{i}{\hbar}(E_n - E_i \pm \hbar\omega_1 \pm \hbar\omega_2 \pm \hbar\omega_3\right).
\end{aligned} \tag{B.24}$$

The transition probability $|a^{(3)}_{n,V_1,V_2,V_3}(t)|^2$ is calculated by

$$\begin{aligned}
|a^{(3)}_{n,V_1,V_2,V_3}(t)|^2 &= (2\pi)^2 \\
&\quad \times \left|\sum_m\sum_{m'}\frac{\langle n|V_3|m'\rangle\langle m'|V_2|m\rangle\langle m|V_1|i\rangle}{(E_m - E_i \pm \hbar\omega_1 - i\hbar\eta_1)(E_{m'} - E_i \pm \hbar\omega_1 \pm \hbar\omega_2 - i\hbar(\eta_1+\eta_2))}\right|^2 \\
&\quad \times \frac{i}{\hbar}\delta(E_n - E_i \pm \hbar\omega_1 \pm \hbar\omega_2 \pm \hbar\omega_3).
\end{aligned} \tag{B.25}$$

In the derivation of Eq. (B.25), we use

$$|\delta(E_n - E_i \pm \hbar\omega_1 \pm \hbar\omega_2 \pm \hbar\omega_3)|^2 = \delta(E_n - E_i \pm \hbar\omega_1 \pm \hbar\omega_2 \pm \hbar\omega_3). \tag{B.26}$$

The factor $2\pi\hbar = \int_{-\infty}^{\infty} dt$ is the time from $-\infty$ to ∞. Thus we can obtain the transition probability from the initial (i) to the final (f) state per unit time $W^{fi(3)}_{V_1,V_2,V_3}$ by dividing Eq. (B.25) by $2\pi\hbar$ as follows:

$$\begin{aligned} W^{fi(3)}_{V_1,V_2,V_3} &= \frac{2\pi}{\hbar} \\ &\times \left| \sum_m \sum_{m'} \frac{\langle f|V_3|m'\rangle\langle m'|V_2|m\rangle\langle m|V_1|i\rangle}{(E_m - E_i \pm \hbar\omega_1 - i\gamma_1)(E_{m'} - E_i \pm \hbar\omega_1 \pm \hbar\omega_2 - i\gamma_2)} \right|^2 \\ &\times \frac{i}{\hbar}\delta(E_f - E_i \pm \hbar\omega_1 \pm \hbar\omega_2 \pm \hbar\omega_3), \end{aligned} \tag{B.27}$$

where we use $\gamma_1 = \hbar\eta_1$ and $\gamma_2 = \hbar(\eta_1 + \eta_2)$. In the first-order Raman scattering, (1) the initial and final states are same ($i = f$), and (2) V_1 (V_3) and V_2 are electron-photon and electron-phonon interaction, respectively, and (3) $+\hbar\omega_1$ corresponds to E_L (optical absorption), $\pm\hbar\omega_2$ corresponds to $\pm\hbar\omega_\nu$ ($+$ ($-$) phonon emission (absorption)), and $+\hbar\omega_3$ corresponds to $-E_s$ (light emission). Thus, we can write the intensity of the first-order Raman spectroscopy as

$$\begin{aligned} I_s &= \sum_\nu \left| \sum_{i=f,m,m'} \frac{M^{fm'}_{opt} M^{m'm}_{ep,\nu} M^{mi}_{opt}}{(E_{\mathrm{L}} - E^{mi} - i\gamma_1)(E_{\mathrm{L}} - E^{m'i} \pm \hbar\omega_\nu - i\gamma_2)} \right|^2 \\ &\times \delta(E_{\mathrm{L}} - E_{\mathrm{S}} \pm \hbar\omega_\nu), \end{aligned} \tag{B.28}$$

where E_{L}, E_{S}, $\hbar\omega_\nu$ are the energy of incident light, scattered light, and the ν mode phonon, respectively, and $E^{m(m')i} = E_{m(m')} - E_i$ is the energy difference between the i and $m(m')$ states.

Publication list

Papers

1. Kunyan Zhang, **Xiaoqi Pang**, Tong Wang, Fei Han, Shun-Li Shang, Nguyen T. Hung, Ahmad R. T. Nugraha, Zi-Kui Liu, Mingda Li, Riichiro Saito, and Shengxi Huang, Anomalous phonon-mode dependence in polarized Raman spectroscopy of the topological Weyl semimetal TaP, Phys. Rev. B 101, 014308, 2020.

Conferences

Oral presentations

1. **X. Pang**, Nguyan T. Hung, A. R. T. Nugraga and R. Saito. First-order polarized Raman spectra of TaP . Presented in ATI Zao-meeting, (August 05-06, 2019), Zao-Yamagata, Japan.

Poster Presentations

1. **X. Pang**, Nguyan T. Hung, A. R. T. Nugraga and R. Saito. First order resonant Raman spectra of TaP. The 56th Fullerenes, Nanotubes and Graphene General Symposium (March 02-04, 2019), Nagoya University, Tokyo, Japan.
2. **X. Pang**, T. Wang, Nguyan T. Hung, A. R. T. Nugraga, K. Zhang, S. Huang and R. Saito. Polarized Raman spectra of TaP. The 3rd Symposium for the Core Research Clusters for Materials Science and Spintronics (February 10-11, 2020), Sendai International Center, Sendai, Japan.

Bibliography

[1] Chandra Shekhar, Ajaya K Nayak, Yan Sun, Marcus Schmidt, Michael Nicklas, Inge Leermakers, Uli Zeitler, Yurii Skourski, Jochen Wosnitza, Zhongkai Liu, et al., Nature Physics 11(8), 645–649 (2015).

[2] Su-Yang Xu, Ilya Belopolski, Nasser Alidoust, Madhab Neupane, Guang Bian, Chenglong Zhang, Raman Sankar, Guoqing Chang, Zhujun Yuan, Chi-Cheng Lee, et al., Science 349(6248), 613–617 (2015).

[3] BQ Lv, HM Weng, BB Fu, XP Wang, Hu Miao, Junzhang Ma, P Richard, XC Huang, LX Zhao, GF Chen, et al., Physical Review X 5(3), 031013 (2015).

[4] LX Yang, ZK Liu, Yan Sun, Han Peng, HF Yang, Teng Zhang, Bo Zhou, Yi Zhang, YF Guo, Marein Rahn, et al., Nature physics 11(9), 728–732 (2015).

[5] Alexey A Soluyanov, Dominik Gresch, Zhijun Wang, QuanSheng Wu, Matthias Troyer, Xi Dai, and B Andrei Bernevig, Nature 527(7579), 495–498 (2015).

[6] Yan Sun, Shu-Chun Wu, Mazhar N Ali, Claudia Felser, and Binghai Yan, Physical Review B 92(16), 161107 (2015).

[7] Yinan Liu, Qiangqiang Gu, Yu Peng, Shaomian Qi, Na Zhang, Yinong Zhang, Xiumei Ma, Rui Zhu, Lianming Tong, Ji Feng, et al., Advanced Materials 30(25), 1706402 (2018).

[8] Kenan Zhang, Changhua Bao, Qiangqiang Gu, Xiao Ren, Haoxiong Zhang, Ke Deng, Yang Wu, Yuan Li, Ji Feng, and Shuyun Zhou, Nature communications 7(1), 1–6 (2016).

[9] Binghai Yan and Claudia Felser, Annual Review of Condensed Matter Physics 8, 337–354 (2017).

[10] ZK Liu, LX Yang, Y Sun, T Zhang, H Peng, HF Yang, C Chen, Y Zhang, YF Guo, Dharmalingam Prabhakaran, et al., Nature materials 15(1), 27–31 (2016).

[11] Hermann Weyl, Proceedings of the National Academy of Sciences of the United States of America 15(4), 323 (1929).

[12] Hongming Weng, Chen Fang, Zhong Fang, B Andrei Bernevig, and Xi Dai, Physical Review X 5(1), 011029 (2015).

[13] Shin-Ming Huang, Su-Yang Xu, Ilya Belopolski, Chi-Cheng Lee, Guoqing Chang, BaoKai Wang, Nasser Alidoust, Guang Bian, Madhab Neupane, Chenglong Zhang, et al., Nature communications 6(1), 1–6 (2015).

[14] Xiaochun Huang, Lingxiao Zhao, Yujia Long, Peipei Wang, Dong Chen, Zhanhai Yang, Hui Liang, Mianqi Xue, Hongming Weng, Zhong Fang, et al., Physical Review X 5(3), 031023 (2015).

[15] Cheng-Long Zhang, Su-Yang Xu, Ilya Belopolski, Zhujun Yuan, Ziquan Lin, Bingbing Tong, Guang Bian, Nasser Alidoust, Chi-Cheng Lee, Shin-Ming Huang, et al., Nature communications 7(1), 1–9 (2016).

[16] Frank Arnold, Chandra Shekhar, Shu-Chun Wu, Yan Sun, Ricardo Donizeth Dos Reis, Nitesh Kumar, Marcel Naumann, Mukkattu O Ajeesh, Marcus Schmidt, Adolfo G Grushin, et al., Nature communications 7, 11615 (2016).

[17] F Widulle, T Ruf, A Göbel, I Silier, E Schönherr, M Cardona, J Camacho, A Cantarero, W Kriegseis, and VI Ozhogin, Physica B: Condensed Matter 263, 381–383 (1999).

[18] JA Freitas Jr and WJ Moore, Brazilian journal of physics 28(1), 12–18 (1998).

[19] E Anastassakis, Lasers in Medical Science 4(1), 41 (1989).

[20] David Tuschel, Spectroscopy 29, 14 (2014).

[21] Kunyan Zhang, Xiaoqi Pang, Tong Wang, Fei Han, Shun-Li Shang, Nguyen T Hung, Ahmad RT Nugraha, Zi-Kui Liu, Mingda Li, Riichiro Saito, et al., Physical Review B 101(1), 014308 (2020).

[22] Paolo Giannozzi, Stefano Baroni, Nicola Bonini, Matteo Calandra, Roberto Car, Carlo Cavazzoni, Davide Ceresoli, Guido L Chiarotti, Matteo Cococcioni, Ismaila Dabo, Andrea Dal Corso, Stefano de Gironcoli, Stefano Fabris, Guido Fratesi, Ralph Gebauer, Uwe Gerstmann, Christos Gougoussis, Anton Kokalj, Michele Lazzeri, Layla Martin-Samos, Nicola Marzari, Francesco Mauri, Riccardo Mazzarello, Stefano Paolini, Alfredo Pasquarello, Lorenzo Paulatto, Carlo Sbraccia, Sandro Scandolo, Gabriele Sclauzero, Ari P Seitsonen, Alexander Smogunov, Paolo Umari, and Renata M Wentzcovitch, J. Phys. Condens. Matter 21(39), 395502 (2009).

[23] S. Poncé, E.R. Margine, C. Verdi, and F. Giustino, Comput. Phys. Commun. 209, 116–133 (2016).

[24] Su-Yang Xu, Ilya Belopolski, Daniel S Sanchez, Chenglong Zhang, Guoqing Chang, Cheng Guo, Guang Bian, Zhujun Yuan, Hong Lu, Tay-Rong Chang, et al., Science advances 1(10), e1501092 (2015).

[25] JP Perdew, ER McMullen, and Alex Zunger, Physical Review A 23(6), 2785 (1981).

[26] Yuki Tatsumi and Riichiro Saito, Physical Review B 97(11), 115407 (2018).